Since January 2020 Elsevier has created a COVID-19 resource centre with free information in English and Mandarin on the novel coronavirus COVID-19. The COVID-19 resource centre is hosted on Elsevier Connect, the company's public news and information website.

Cell

SARS-CoV-2 Infection Depends on Cellular Heparan Sulfate and ACE2

Graphical Abstract

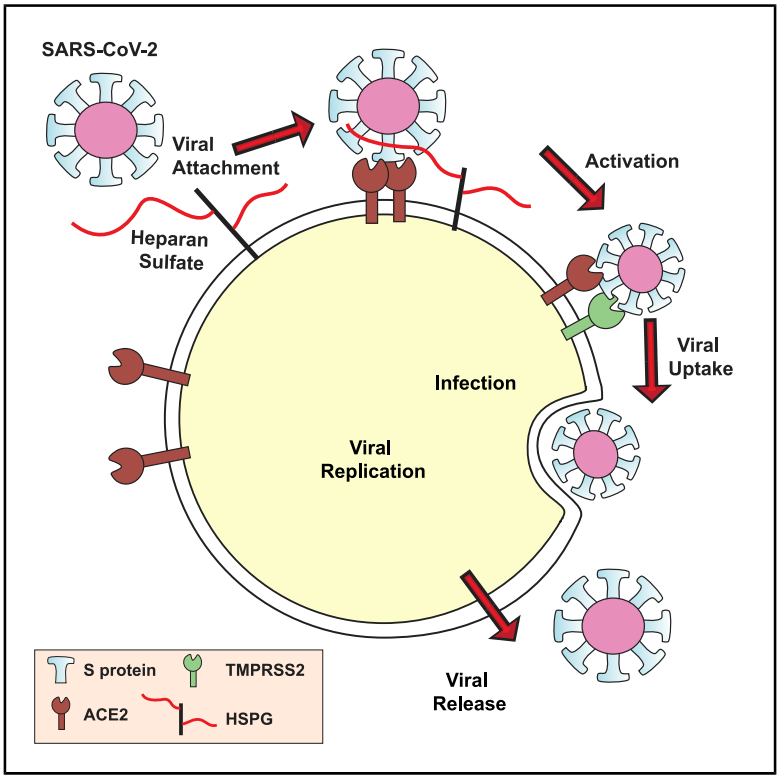

Highlights

- SARS-CoV-2 spike protein interacts with heparan sulfate and ACE2 through the RBD
- Heparan sulfate promotes Spike-ACE2 interaction
- SARS-CoV-2 infection is co-dependent on heparan sulfate and ACE2
- Heparin and non-anticoagulant derivatives block SARS-CoV-2 binding and infection

Authors

Thomas Mandel Clausen, Daniel R. Sandoval, Charlotte B. Spliid, ..., Andrew B. Ward, Aaron F. Carlin, Jeffrey D. Esko

Correspondence

tmandelclausen@health.ucsd.edu (T.M.C.), jesko@health.ucsd.edu (J.D.E.)

In Brief

Clausen et al. provide evidence that heparan sulfate is a necessary co-factor for SARS-CoV-2 infection. They show that heparan sulfate interacts with the receptor-binding domain of the SARS-CoV-2 spike glycoprotein, adjacent to ACE2, shifting the spike structure to an open conformation to facilitate ACE2 binding.

Clausen et al., 2020, Cell *183*, 1043–1057
November 12, 2020
https://doi.org/10.1016/j.cell.2020.09.033

CellPress

Cell

CellPress

Article

SARS-CoV-2 Infection Depends on Cellular Heparan Sulfate and ACE2

Thomas Mandel Clausen,[1,2,18,19,20,*] Daniel R. Sandoval,[1,19] Charlotte B. Spliid,[1,2,18] Jessica Pihl,[1,2,18] Hailee R. Perrett,[3] Chelsea D. Painter,[1,4] Anoop Narayanan,[5] Sydney A. Majowicz,[5] Elizabeth M. Kwong,[6] Rachael N. McVicar,[6] Bryan E. Thacker,[7] Charles A. Glass,[7] Zhang Yang,[8] Jonathan L. Torres,[3] Gregory J. Golden,[1,4] Phillip L. Bartels,[1,17] Ryan N. Porell,[9] Aaron F. Garretson,[10] Logan Laubach,[9] Jared Feldman,[11] Xin Yin,[12] Yuan Pu,[12] Blake M. Hauser,[11] Timothy M. Caradonna,[11] Benjamin P. Kellman,[13,14,15] Cameron Martino,[13,14] Philip L.S.M. Gordts,[10,17] Sumit K. Chanda,[12] Aaron G. Schmidt,[11,16] Kamil Godula,[9,17] Sandra L. Leibel,[14] Joyce Jose,[5] Kevin D. Corbett,[1] Andrew B. Ward,[3] Aaron F. Carlin,[10] and Jeffrey D. Esko[1,17,*]

[1]Department of Cellular and Molecular Medicine, University of California, San Diego, La Jolla, CA 92093, USA
[2]Department for Immunology and Microbiology, Faculty of Health and Medical Sciences, University of Copenhagen, 2200 Copenhagen, Denmark
[3]Department of Integrative Structural and Computational Biology, The Scripps Research Institute, La Jolla, CA 92037, USA
[4]Biomedical Sciences Graduate Program, University of California San Diego, La Jolla, California, USA
[5]Department of Biochemistry and Molecular Biology, The Huck Institutes of the Life Sciences, Pennsylvania State University, University Park, PA 16802, USA
[6]Sanford Burnham Prebys Medical Discovery Institute, La Jolla, CA 92037, USA
[7]TEGA Therapeutics, Inc., 3550 General Atomics Court, G02-102, San Diego, CA 92121, USA
[8]Copenhagen Center for Glycomics, Department of Molecular and Cellular Medicine, University of Copenhagen, 2200 Copenhagen, Denmark
[9]Department of Chemistry and Biochemistry, University of California, San Diego, La Jolla, CA 92093, USA
[10]Department of Medicine, University of California, San Diego, La Jolla, CA 92037, USA
[11]Ragon Institute of MGH, MIT and Harvard, Cambridge, MA 02139, USA
[12]Immunity and Pathogenesis Program, Infectious and Inflammatory Disease Center, Sanford Burnham Prebys Medical Discovery Institute, 10901 North Torrey Pines Road, La Jolla, CA 92037, USA
[13]Department of Bioengineering, University of California, San Diego, La Jolla, CA 92093, USA
[14]Department of Pediatrics, University of California San Diego School of Medicine, La Jolla, CA 92093, USA
[15]Bioinformatics and Systems Biology Program, University of California, San Diego, La Jolla, CA 92093, USA
[16]Department of Microbiology, Harvard Medical School, Boston, MA 02115, USA
[17]Glycobiology Research and Training Center, University of California, San Diego, La Jolla, CA 92093, USA
[18]Department of Infectious Disease, Copenhagen University Hospital, 2200 Copenhagen, Denmark
[19]These authors contributed equally
[20]Lead Contact
*Correspondence: tmandelclausen@health.ucsd.edu (T.M.C.), jesko@health.ucsd.edu (J.D.E.)
https://doi.org/10.1016/j.cell.2020.09.033

SUMMARY

We show that SARS-CoV-2 spike protein interacts with both cellular heparan sulfate and angiotensin-converting enzyme 2 (ACE2) through its receptor-binding domain (RBD). Docking studies suggest a heparin/heparan sulfate-binding site adjacent to the ACE2-binding site. Both ACE2 and heparin can bind independently to spike protein *in vitro*, and a ternary complex can be generated using heparin as a scaffold. Electron micrographs of spike protein suggests that heparin enhances the open conformation of the RBD that binds ACE2. On cells, spike protein binding depends on both heparan sulfate and ACE2. Unfractionated heparin, non-anticoagulant heparin, heparin lyases, and lung heparan sulfate potently block spike protein binding and/or infection by pseudotyped virus and authentic SARS-CoV-2 virus. We suggest a model in which viral attachment and infection involves heparan sulfate-dependent enhancement of binding to ACE2. Manipulation of heparan sulfate or inhibition of viral adhesion by exogenous heparin presents new therapeutic opportunities.

INTRODUCTION

The COVID-19 pandemic, caused by SARS-CoV-2, has swept across the world, resulting in serious clinical morbidities and mortality, as well as widespread disruption to all aspects of society. As of September 1, 2020, the virus has spread to 215 countries, causing more than 25.4 million confirmed infections and at least 851,000 deaths (World Health Organization). Current isolation/social-distancing strategies seek to flatten the infection curve to avoid overwhelming hospitals and to give the medical

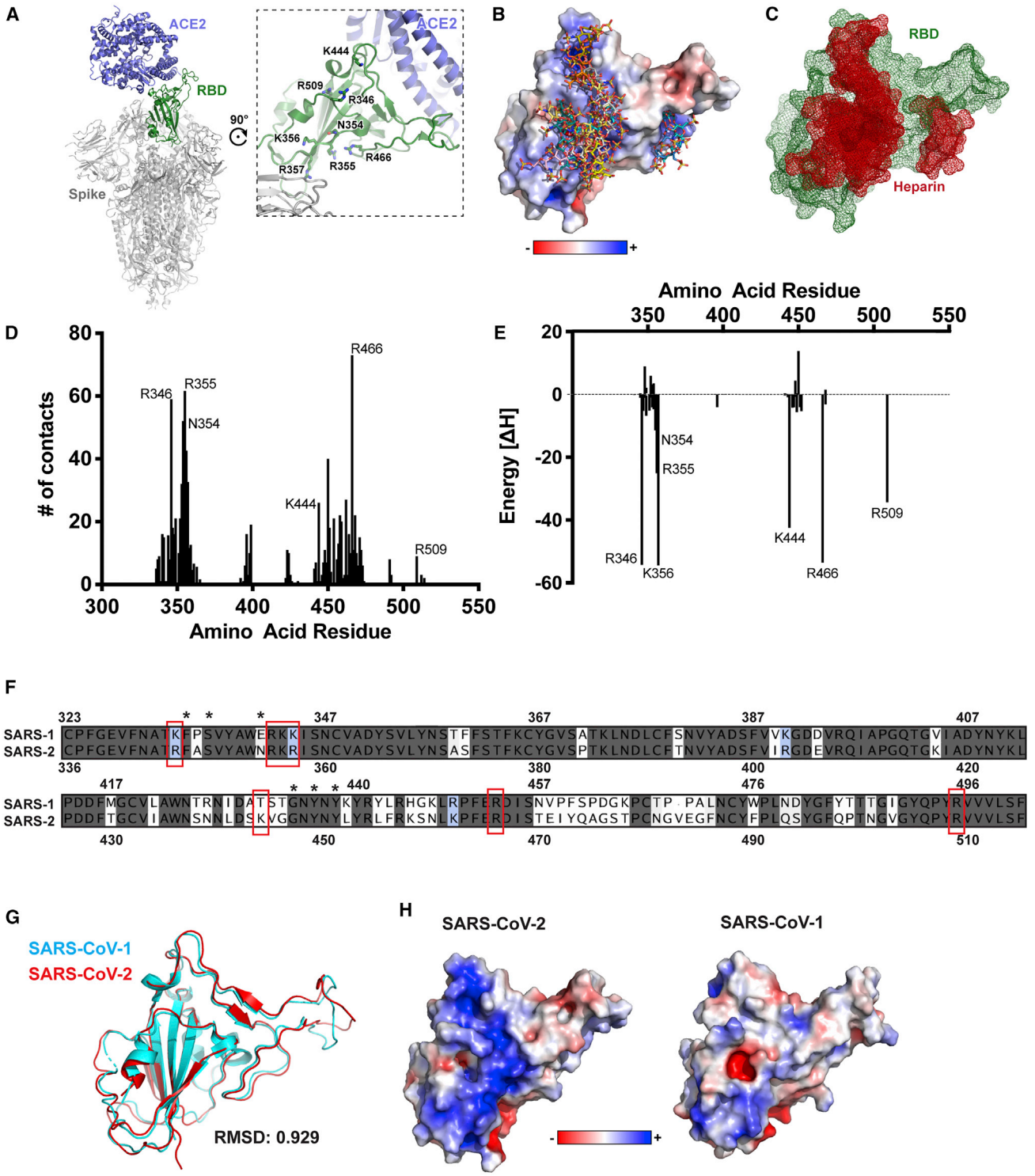

Figure 1. Molecular Modeling of the SARS-Cov-2 Spike RBD Interaction with Heparin

(A) A molecular model of SARS CoV-2 S protein trimer (PDB: 6VSB and 6M0J) rendered with Pymol. ACE2 is shown in blue and the RBD open conformation in green. A set of positively charged residues lies distal to the ACE2 binding site.

(B) Electrostatic surface rendering of the SARS-CoV-2 RBD (PDB: 6M17) docked with dp4 heparin oligosaccharides. Blue and red surfaces indicate electropositive and electronegative surfaces, respectively. Oligosaccharides are represented using standard CPK format.

(C) Mesh surface rendering of the RBD (green) docked with dp4 heparin oligosaccharides (red).

(legend continued on next page)

establishment and pharmaceutical companies time to develop and test antiviral drugs and vaccines. Currently, only one antiviral agent, Remdesivir, has been approved for adult COVID-19 patients (Beigel et al., 2020), and vaccines may be 6–12 months away. Understanding the mechanism for SARS-CoV-2 infection and its mechanism of infection could reveal other targets to interfere with viral infection and spread.

The glycocalyx is a complex mixture of glycans and glycoconjugates surrounding all cells. Given its location, viruses and other infectious organisms must pass through the glycocalyx to engage receptors thought to mediate viral entry into host cells. Many viral pathogens have evolved to utilize glycans as attachment factors, which facilitates the initial interaction with host cells, including influenza virus, herpes simplex virus, human immunodeficiency virus, and different coronaviruses (SARS-CoV-1 and MERS-CoV) (Cagno et al., 2019; Koehler et al., 2020; Stencel-Baerenwald et al., 2014). Several viruses interact with sialic acids, which are located on the ends of glycans found in glycolipids and glycoproteins. Other viruses interact with heparan sulfate (HS) (Milewska et al., 2014), a highly negatively charged linear polysaccharide that is attached to a small set of membrane or extracellular matrix proteoglycans (Lindahl et al., 2015). In general, glycan-binding domains on membrane proteins of the virion envelope mediate initial attachment of virions to glycan receptors. Attachment in this way can lead to the engagement of protein receptors on the host plasma membrane that facilitate membrane fusion or engulfment and internalization of the virion.

Like other macromolecules, HS can be divided into subunits, which are operationally defined as disaccharides based on the ability of bacterial enzymes or nitrous acid to cleave the chain into disaccharide units (Esko and Selleck, 2002). The basic disaccharide subunit consists of β1–4 linked D-glucuronic acid (GlcA) and α1–4 linked *N*-acetyl-D-glucosamine (GlcNAc), which undergo various modifications by sulfation and epimerization as the copolymer assembles on a limited number of membrane and extracellular matrix proteins (only 17 HS proteoglycans are known) (Lindahl et al., 2015). The variable length of the modified domains and their pattern of sulfation create unique motifs to which HS-binding proteins (HSBPs) interact (Xu and Esko, 2014). Different tissues and cell types vary in the structure of HS, and HS structure can vary between individuals and with age (de Agostini et al., 2008; Feyzi et al., 1998; Han et al., 2020; Ledin et al., 2004; Vongchan et al., 2005; Warda et al., 2006; Wei et al., 2011). These differences in HS composition may contribute to the tissue tropism and/or host susceptibility to infection by viruses and other pathogens.

In this report, we show that the ectodomain of the SARS-CoV-2 spike (S) protein interacts with cell surface HS through the receptor-binding domain (RBD) in the S1 subunit. Binding of heparin to SARS-CoV-2 S protein shifts the structure to favor the RBD open conformation that binds ACE2. S binding to cells requires engagement of both cellular HS and ACE2, suggesting that HS acts as a coreceptor priming the S for ACE2 interaction. Therapeutic unfractionated heparin (UFH), non-anticoagulant heparin, and HS derived from human lung and other tissues block binding. UFH and heparin lyases also block infection of cells by S protein pseudotyped virus and authentic SARS-CoV-2. These findings identify cellular HS as a necessary co-factor for SARS-CoV-2 infection and emphasizes the potential for targeting S protein-HS interactions to attenuate virus infection.

RESULTS

Molecular Modeling Reveals an HS-Binding Site Adjacent to the ACE2-Binding Domain in the SARS-CoV-2 Spike Protein

The trimeric S proteins from SARS-CoV-1 and SARS-CoV-2 viruses are thought to engage human ACE2 with one or more RBDs in an "open" active conformation (Figure 1A) (Kirchdoerfer et al., 2018; Walls et al., 2020; Wrapp et al., 2020). Adjacent to the ACE2-binding site and exposed in the RBD lies a group of positively charged amino acid residues that represents a potential site that could interact with heparin or HS (Figures 1A and S1). We calculated an electrostatic potential map of the RBD (from PDB ID 6M17 [Yan et al., 2020]), which revealed an extended electropositive surface with dimensions and turns/loops consistent with a heparin-binding site (Figure 1B) (Xu and Esko, 2014). Docking studies using a tetrasaccharide (dp4) fragment derived from heparin demonstrated preferred interactions with this electropositive surface, which, based on its dimensions, could accommodate a chain of up to 20 monosaccharides (Figures 1B and 1C). Evaluation of heparin-protein contacts and energy contributions using the Molecular Operating Environment (MOE) software suggested strong interactions with the positively charged amino acids R346, R355, K444, R466, and possibly R509 (Figures 1A, 1D, and 1E). Other amino acids, notably F347, S349, N354, G447, Y449, and Y451, could coordinate the oligosaccharide through hydrogen bonds and hydrophobic interactions. Notably, the putative binding surface for oligosaccharides is adjacent to, but separate from, the ACE2-binding site, suggesting that a single RBD could simultaneously bind both cell surface HS and the ACE2 protein receptor. The putative HS-binding site is partially obstructed in the "closed" inactive RBD conformation while fully exposed in the open state (Figure S1).

The amino acid sequence of S protein RBD of SARS-CoV-2 S is 73% identical to the RBD of SARS-CoV-1 S (Figure 1F), and these domains are highly similar in structure with an overall Cα

(D) Number of contacts between the RBD amino acids and a set of docked heparin dp4 oligosaccharides from (A and B).
(E) Calculated energy contributions of each amino acid residue in the RBD that can interact with heparin.
(F) Amino acid sequence alignment of the SARS-CoV-1 and SARS-Cov-2 RBD. Red boxes indicate amino acid residues contributing to the electropositive patch in (A and B). Identical residues are shaded dark gray. Conservative substitutions have backgrounds in blue. Non-conserved residues have a white background
(G) Structural alignment of SARS-CoV-1 (cyan; PDB: 3BGF) and SARS-CoV-2 (red; PDB: 6M17) RBD.
(H) Electrostatic surface rendering of the SARS-CoV-1 and SAR-CoV-2 RBDs.
See also Figure S1.

RMSD of 0.929 Å (Figure 1G). However, an electrostatic potential map of the SARS-CoV-1 S RBD does not show an electropositive surface like that observed in SARS-CoV-2 (Figure 1H). Most of the positively charged residues comprising this surface are conserved between the two proteins, with the exception of SARS-CoV-2 K444, which is a threonine in SARS-CoV-1 (Figure 1F). Additionally, the other amino acid residues predicted to coordinate with the oligosaccharide are conserved with the exception of Asn354 in SARS-CoV-2, which is a negatively charged glutamate residue in SARS-CoV-1. SARS-CoV-1 has been shown to interact with cellular HS in addition to its entry receptors ACE2 and transmembrane protease, serine 2 (TMPRSS2) (Lang et al., 2011). Our analysis suggests that the putative heparin-binding site in SARS-CoV-2 S may mediate an enhanced interaction with heparin or HS compared to SARS-CoV-1, and that this change evolved through as few as two amino acid substitutions, Thr→Lys444 and Glu→Asn354.

The SARS-CoV-2 Spike Protein Binds Heparin through the RBD

To test experimentally if the SARS-CoV-2 S protein interacts with heparin/HS, recombinant ectodomain and RBD proteins were prepared and characterized. Initial studies encountered difficulty in stabilizing the S ectodomain protein, a problem that was resolved by raising the concentration of NaCl to 0.3 M in HEPES (4-(2-hydroxyethyl)-1-piperazineethanesulfonic acid) buffer. Under these conditions, the protein could be stored at room temperature, 4°C, or at −80°C for at least 2 weeks. SDS-PAGE showed that each protein was ~98% pure (Figure S2A). Transmission electron micrographs of the S ectodomains revealed trimeric structures (Figure S2B). The main component by size exclusion chromatography behaved as a glycosylated trimer with an apparent molecular mass of ~740 kDa (Figure S2C). A highly purified commercial preparation of RBD protein was used in some studies (SINO Biologics, Figure S2A), as well as recombinant RBD protein expressed in ExpiHEK cells (Figure S2D), both of which were judged >98% pure by SDS-PAGE and size exclusion chromatography (Figure S2E).

Recombinant S ectodomain and RBD proteins were applied to a column of heparin-Sepharose. Elution with a gradient of sodium chloride showed that the RBD eluted at ~0.3 M NaCl, with a shoulder that eluted with higher salt (Figure 2A). Recombinant S ectodomain also bound to heparin-Sepharose, but it eluted across a broader concentration of NaCl. The elution profiles suggest that the preparations contained a population of molecules that bind to heparin, but that some heterogeneity in affinity for heparin occurs, which may reflect differences in glycosylation, oligomerization, or the number of binding sites in the open conformation.

The RBD protein from SARS-CoV-2 also bound in a saturable manner to heparin-BSA immobilized on a plate (Figure 2B). The RBD from SARS-CoV-1 showed significantly reduced binding to heparin-BSA and a higher K_D value (640 nM [95% CI; 282–1852 nM] for SARS-CoV-1 RBD versus 150 nM [95% CI; 123–173 nM]) for SARS-CoV-2 RBD), in accordance with the difference in electropositive potential in the proposed HS-binding regions (Figure 1H). A monomeric form of SARS-CoV-2 S ectodomain protein also bound in a saturable manner to heparin immobilized on a plate (Figure S3A). The trimeric protein bound to heparin-BSA with an apparent K_D value of 3.8 nM (95% CI; 3.1–4.6 nM) (Figure 2C). Binding of recombinant S ectodomain, mutated to lock the RBDs into a closed (Mut2), or one that favors an open (Mut7) conformation, showed that the heparin-binding site in the RBD is accessible in both conformations (Figure 2D). However, the K_D value for Mut7 is lower (4.6 nM [95% CI; 3.8–5.5 nM] versus 9.9 nM [95% CI; 8.7–11.3 nM] for Mut2), which is in line with the partial obstruction of the site in the closed conformation (Figure S1). As expected, only S trimers with an open RBD conformation bound to ACE2 (Figure 2E).

In contrast to S protein, ACE2 did not bind to heparin-BSA (Figure 2C). ACE2 also had no effect on binding of S protein to heparin-BSA at all concentrations that were tested (Figure 2C, inset). Biotinylated ACE2 bound to immobilized S protein (Figure S3B), and a ternary complex of heparin, ACE2, and S protein could be demonstrated by titration of S protein bound to immobilized heparin-BSA with ACE2 (Figure 2F). Binding of ACE2 under these conditions increased in proportion to the amount of S protein bound to the heparin-BSA. Collectively, these findings show that (1) S protein can engage both heparin and ACE2 simultaneously and (2) that the heparin-binding site is somewhat occluded in the closed conformation, but it can still bind heparin, albeit with reduced affinity.

SARS-CoV-2 Protein Binding to Heparin Increases ACE2 Occupancy of RBDs

The simultaneous binding of ACE2 to S protein and heparin suggested the possibility that heparin binding might affect the conformation of the RBD, possibly increasing the open conformation that can bind ACE2. To explore this possibility, S protein was mixed with ACE2 (6-fold molar ratio) with or without dp20 oligosaccharides derived from heparin (9-fold molar ratio). The samples were then stained and analyzed by transmission electron microscopy, and the images were deconvoluted and sorted into 3D reconstructions to determine the number of trimers with zero, one, two, or three bound ACE2 (Figures 2G, 2H, S3C, and S3D). The different populations were counted and the percentage of particles belonging to each 3D class was calculated. Two time points were evaluated after mixing ACE2 and trimeric S: at 15 min, 29,600 and 31,300 particles were analyzed in the absence or presence of dp20 oligosaccharides, respectively; at 60 min, 17,000 and 21,000 particles were analyzed in absence or presence of dp20 oligosaccharides, respectively. At both time points, the presence of dp20 increased the total amount of ACE2 protein bound to S (Figures 2G and 2H). After 15 min in the absence of dp20, very few of the trimers had conformations with one or two bound ACE2 (5% each), whereas the inclusion of dp20 oligosaccharides greatly increased the proportion of trimers bearing one (37%) or two (21%) ACE2, with a proportional drop in the unbound conformers from 90% in the absence of heparin to 42% in its presence (Figure 2G). Extending the incubation to 60 min resulted in a mixture of trimers containing one (45%), two (11%), and three ACE2 (13%) in the absence of heparin. Inclusion of dp20 further increased the proportion of bound S trimers bearing two (19%) and three (27%) ACE2 (Figure 2H). The imaging studies suggest that, under these experimental conditions, heparin may stabilize the ACE2 interaction, increasing the proportion of S bound to ACE2 as well as the occupancy of individual S proteins.

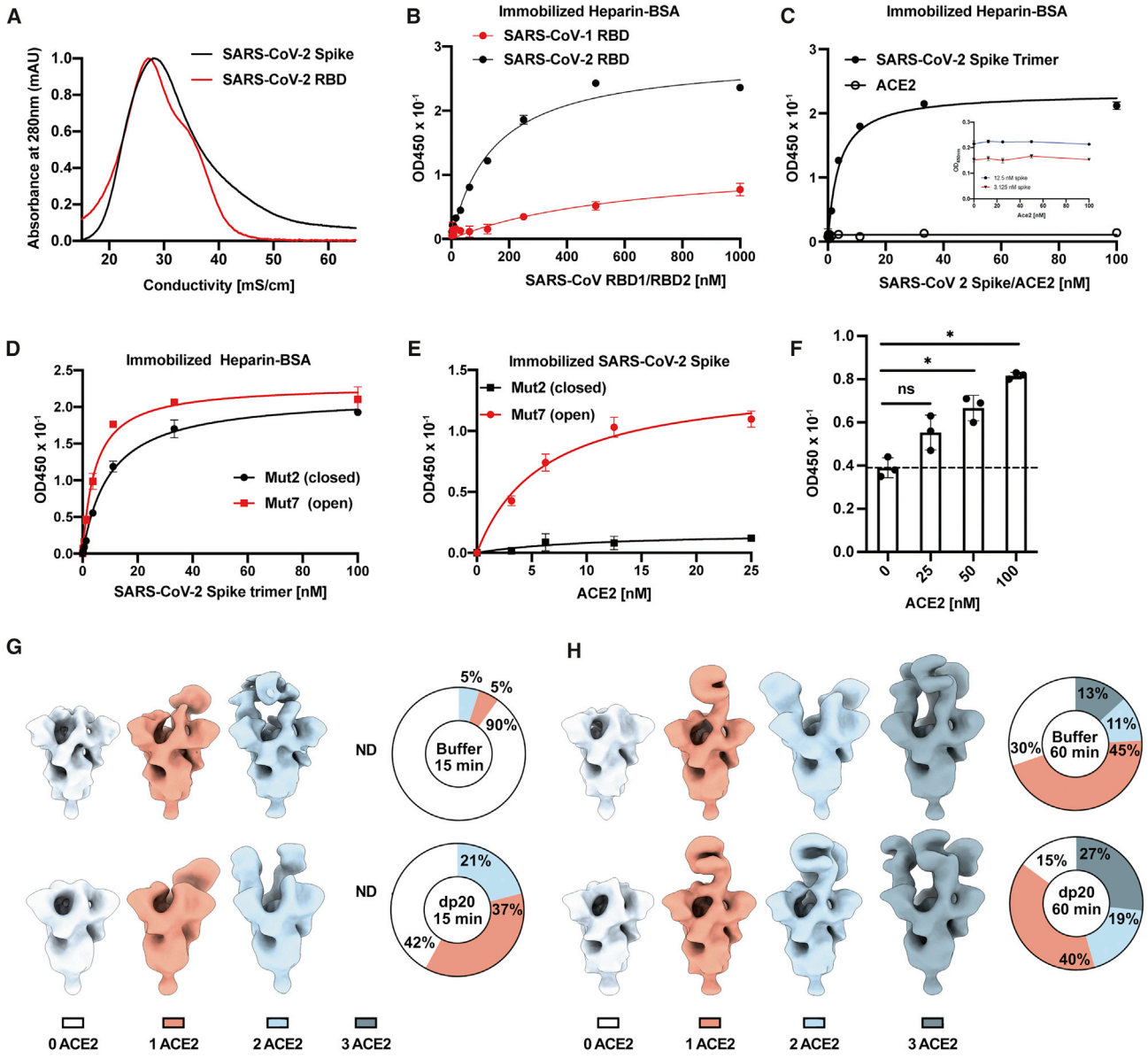

Figure 2. SARS-CoV-2 Spike Binds Heparin through the RBD

(A) Recombinant trimeric SARS-CoV-2 spike and RBD proteins were bound to heparin-Sepharose and eluted with a gradient of sodium chloride.

(B) RBD protein from SARS-CoV-1 and SARS-CoV-2 binding to immobilized heparin-BSA.

(C) Binding of spike protein or ACE2 to heparin-BSA. Insert shows SARS-CoV-2 spike protein binding to heparin-BSA in the presence of ACE2.

(D) Binding of spike protein in the active RBD open (Mut7) and inactive RBD closed (Mut2) conformation to heparin-BSA.

(E) Binding of ACE2 to spike protein in active RBD open (Mut7) and inactive RBD closed (Mut 2) conformation.

(F) ACE2 binding to spike protein immobilized on heparin-BSA. The broken line represents background binding. Statistical analysis was by one-way ANOVA. (ns: $p > 0.05$, *: $p \leq 0.05$, **: $p \leq 0.01$, ***: $p \leq 0.001$, ****: $p \leq 0.0001$).

(G and H) Negative stain-electron microscopy analysis of binding of heparin and ACE2 to spike protein. ACE2 binding to spike protein increases in the presence of heparin. 3D class averages of SARS-CoV-2 spike bound to zero, one, two, or three ACE2 (white, orange, blue, or gray) when complexed with and without a heparin dp20. The incubation was done for 15 min (G) or 60 min (H). The percentage of particles belonging to each class is shown in pie charts.

See also Figure S3.

The SARS-CoV-2 Spike Protein Depends on Cellular Heparan Sulfate for Cell Binding

To extend these studies to HS on the surface of cells, S ectodomain protein was added to human H1299 cells, an adenocarcinoma cell line derived from type 2 alveolar cells (Figure 3A). S ectodomains bound to H1299 cells, with half-maximal binding achieved at ~75 nM. Treatment of the cells with a mixture of heparin lyases (HSase), which degrades cell surface HS,

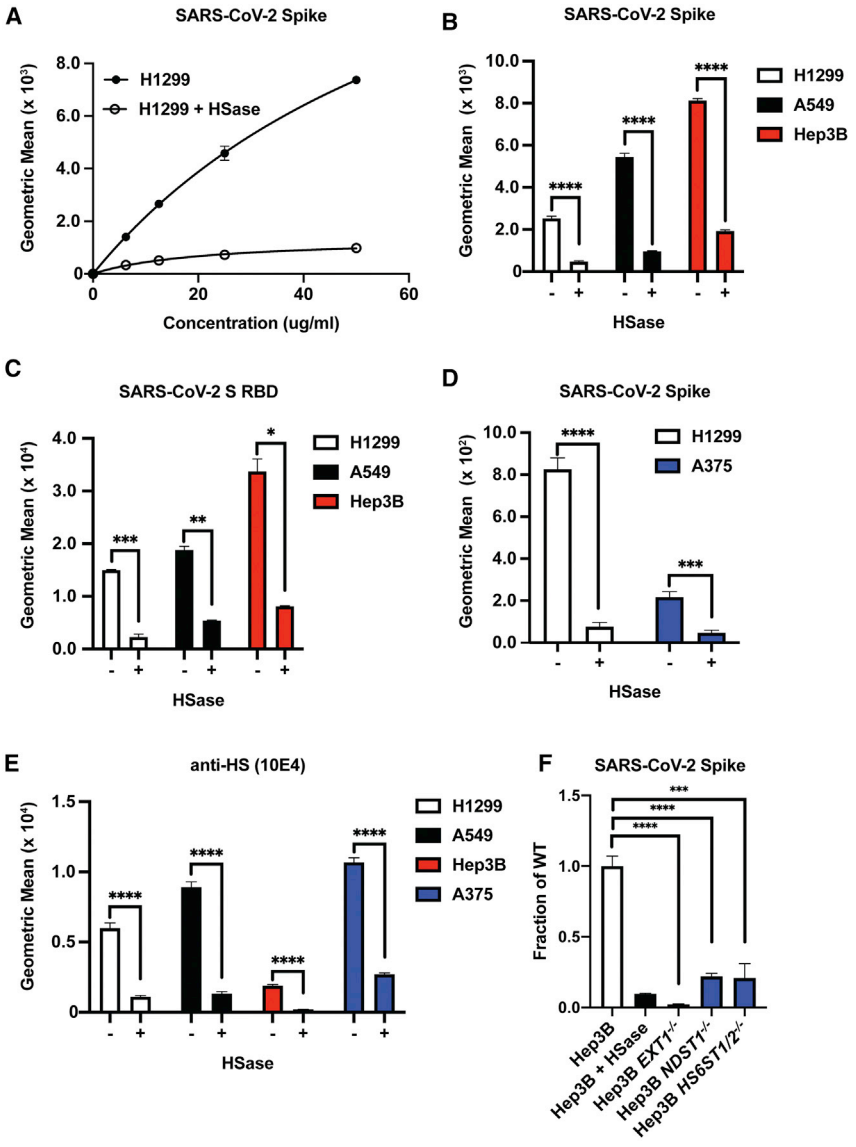

Figure 3. SARS-CoV-2 Spike Ectodomain Binding to Cells Is Dependent on Cellular HS

(A) Titration of recombinant SARS-CoV-2 spike protein binding to human H1299 cells with and without treatment with a mix of heparin lyases I, II, and III (HSase).

(B) Recombinant SARS-CoV-2 spike protein binding (20 μg/mL) to H1299, A549, and Hep3B cells with and without HSase treatment.

(C) SARS-CoV-2 S RBD protein binding (20 μg/mL) to H1299, A549, and Hep3B cells with and without HSase treatment.

(D) SARS-CoV-2 spike protein binding (20 μg/mL) to H1299 and A375 cells with and without HSase treatment.

(E) Anti-HS (F58-10E4) staining of H1299, A549, Hep3B, and A375 cells with and without HSase treatment.

(F) Binding of recombinant SARS-CoV-2 spike protein (20 μg/mL) to Hep3B mutants altered in HS biosynthesis enzymes. Specific enzymes that were lacking in the mutants are listed along the x axis. All values were obtained by flow cytometry. Graphs shows representative experiments performed in technical triplicate. The experiments were repeated at least three times. Statistical analysis by unpaired t test (ns: $p > 0.05$, *: $p \leq 0.05$, **: $p \leq 0.01$, ***: $p \leq 0.001$, ****: $p \leq 0.0001$).

See also Figure S4.

dramatically reduced binding (Figure 3A). The S ectodomain also bound to human A549 cells, another type 2 alveolar adenocarcinoma line, as well as human hepatoma Hep3B cells (Figure 3B). Removal of HS by enzymatic treatment dramatically reduced binding in both of these cell lines as well (Figure 3B). Recombinant RBD protein also bound to all three cell lines dependent on HS (Figure 3C). A melanoma cell line, A375, was tested independently and also showed HS-dependent binding (Figure 3D). The extent of binding across the four cell lines varied ~4-fold. This variation was not due to differences in HS expression as illustrated by staining of cell surface HS with mAb 10E4, which recognizes a common epitope in HS (Figure 3E). In fact, A375 cells have the highest expression of cell surface HS but the lowest extent of S protein binding (Figure 3D), whereas Hep3B cells have low amounts of cell surface HS and the highest binding of S protein. This lack of correlation could reflect differences in the structure of HS or the level of expression of ACE2.

We also measured binding of the S ectodomain and RBD proteins to a library of mutant Hep3B cells, carrying CRISPR-Cas9-induced mutations in biosynthetic enzymes essential for synthesizing HS (Anower-E-Khuda et al., 2019). Inactivation of *EXT1*, a subunit of the copolymerase required for synthesis of the backbone of HS, abolished binding to a greater extent than enzymatic removal of the chains with HSases (Figures 3F and S4), suggesting that the HSase treatment may underestimate the dependence on HS. Targeting *NDST1*, a GlcNAc *N*-deacetylase-*N*-sulfotransferase that N-deacetylates and N-sulfates *N*-acetylglucosamine residues, and *HS6ST1* and *HS6ST2*, which introduces sulfate groups in the C6 position of glucosamine residues, significantly reduced binding (Figures 3F and S4). Although experiments with other sulfotransferases have not yet been done, the data suggest that the pattern of sulfation of HS affects binding to S and RBD.

Heparin and Heparan Sulfates Inhibit Binding of Spike Ectodomain Protein

To further examine how variation in HS structure affects binding, we isolated HS from human kidney, liver, lung, and tonsil. The samples were depolymerized into disaccharides by treatment with HSases, and the disaccharides were then analyzed by LC-MS/MS. The disaccharide analysis showed that lung HS has a larger proportion of *N*-deacetylated and *N*-sulfated glucosamine residues (gray bars) and more 2-*O*-sulfated uronic

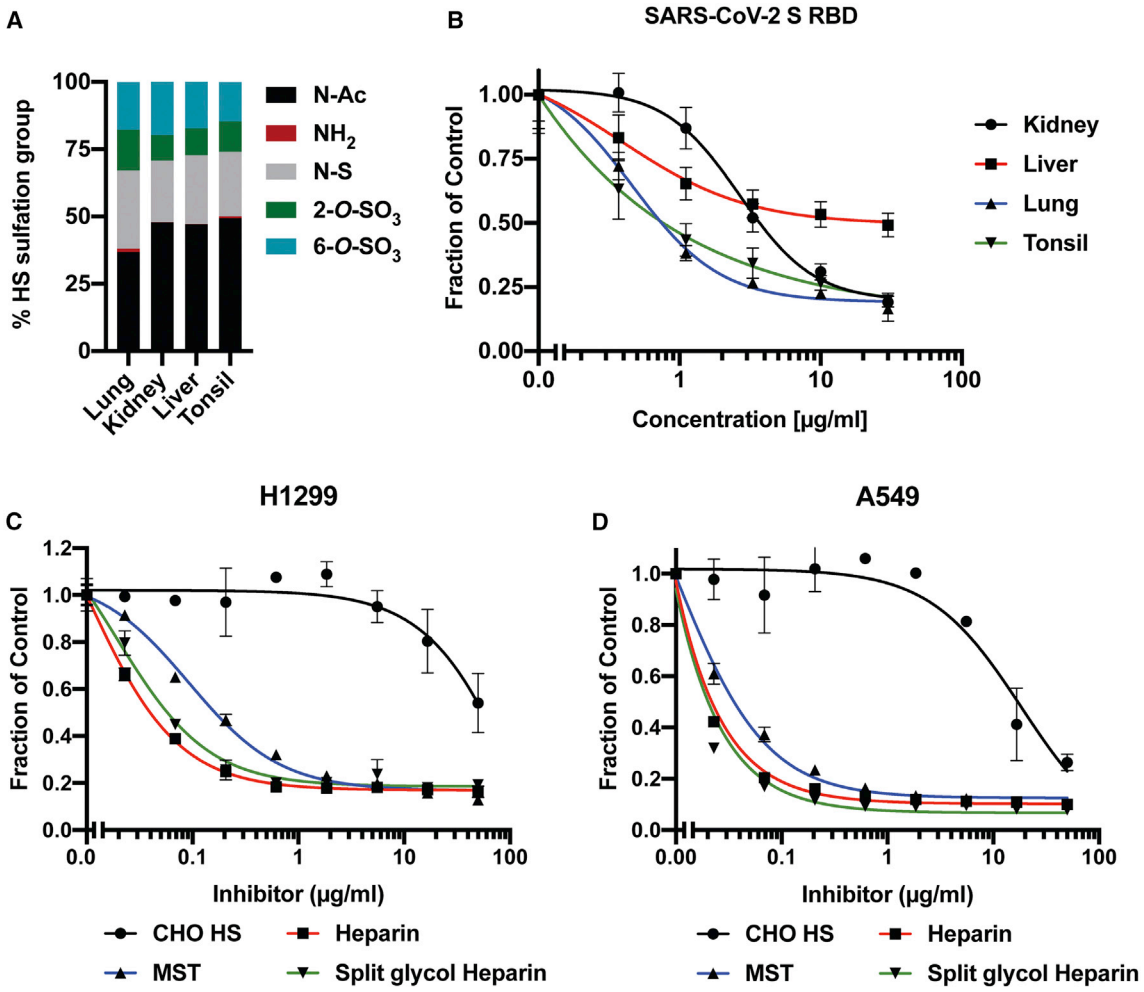

Figure 4. SARS-CoV-2 Spike Ectodomain Protein Binding to Cells Is Differentially Affected by HS from Different Organs and Potently Inhibited by Heparinoids

(A) LC-MS/MS disaccharide analysis of HS isolated from human kidney, liver, tonsil, and lung tissue.

(B) Inhibition of binding of recombinant SARS-CoV-2 S RBD protein to H1299 cells, using tissue HS. Analysis by flow cytometry.

(C) Inhibition of recombinant trimeric SARS-CoV-2 protein (20 μg/mL) binding to H1299 cells, using CHO HS, heparin, MST heparin, and split-glycol heparin. Analysis by flow cytometry.

(D) Similar analysis of A549 cells. Curve fitting was performed using non-linear regression and the inhibitor versus response least-squares fit algorithm. IC_{50} values are listed in Table 1. Graphs show representative experiments performed in technical duplicates or triplicates. (ns: $p > 0.05$, *: $p \leq 0.05$, **: $p \leq 0.01$, ***: $p \leq 0.001$, ****: $p \leq 0.0001$).

acids (green bars) than HS preparations from the other tissues (Figure 4A). The different HS preparations also varied in their ability to block binding of RBD to H1299 cells (Figure 4B). Interestingly, HS isolated from lung was more potent compared to kidney and liver HS, consistent with the greater degree of sulfation of HS from this organ (Table 1). HS from tonsil was as potent as HS from lung, but the overall extent of sulfation was not as great, supporting the notion that the patterning of the sulfated domains in the chains may affect binding.

UFH is derived from porcine mucosa and possesses potent anticoagulant activity due to the presence of a pentasaccharide sequence containing a crucial 3-*O*-sulfated *N*-sulfoglucosamine unit, which confers high-affinity binding to antithrombin. Heparin is also very highly sulfated compared to HS, with an average negative charge of –3.4 per disaccharide (the overall negative charge density of typical HS is –1.8 to –2.2 per disaccharide). MST cells, which were derived from a murine mastocytoma, make heparin-like HS that lacks the key 3-*O*-sulfate group and anticoagulant activity (Gasimli et al., 2014; Montgomery et al., 1992). The anticoagulant properties of heparin can also be removed by periodate oxidation, which oxidizes the vicinal hydroxyl groups in the uronic acids, resulting in what is called "split-glycol" heparin (Casu et al., 2004). All of these agents significantly inhibited binding of the S protein to H1299 and A549 cells (Figures 4C and 4D) yielding IC_{50} values in the range of 0.01–0.12 μg/mL (Table 1). Interestingly, the lack of 3-*O*-sulfation, crucial for the anticoagulant activity of heparin, had little effect on its inhibition of S binding. In

Table 1. IC_{50} Values for Heparin and HS as Competitive Inhibitors of S Protein Binding

Cells	Inhibitor	IC_{50} (μg/mL)	95% CI (μg/mL)	R^2 of fit
H1299	CHO HS	139	18–∞	0.803
	heparin	0.03	0.02–0.04	0.991
	MST heparin	0.12	0.09–0.15	0.991
	split-glycol heparin	0.04	0.03–0.06	0.971
	kidney HS	8.4	3.7–25	0.749
	liver HS	62	15–∞	0.627
	lung HS	2.1	0.78–5.8	0.828
	tonsil HS	2.5	0.74–7.5	0.838
A549	CHO HS	19	8.6–49	0.907
	heparin	0.01	0.010–0.013	0.997
	MST heparin	0.03	0.026–0.032	0.997
	split-glycol heparin	0.01	0.007–0.008	0.999

IC_{50} values and confidence intervals were determined using non-linear regression using the inhibitor versus response least-squares fit algorithm. Related to Figure 4.

contrast, CHO cell HS (containing 0.8 sulfates per disaccharide) only weakly inhibited binding (IC_{50} values of 18 and 139 μg/mL for A549 and H1299, respectively) (Table 1). These data suggest that inhibition by heparinoids is most likely charge dependent and independent of anticoagulant activity per se.

Binding of Spike Protein to ACE2 Also Depends on Heparan Sulfate

The experiments shown in Figures 2G and 2H indicate that binding of heparin to S protein can increase binding to ACE2. To explore if HS, ACE2, and S interact at the cell surface, we investigated the impact of ACE2 expression on S protein cell binding. Initial attempts were made to measure ACE2 levels by western blotting or flow cytometry with different mAbs and polyclonal antibodies, but a reliable signal was not obtained in any of the cell lines tested (A375, A549, H1299, and Hep3B). Nevertheless, expression of ACE2 mRNA was observed by qRT-PCR (Figure S5A). Transfection of A375 cells with ACE2 cDNA resulted in robust expression of ACE2 (Figure 5A), resulting in an increase in S ectodomain protein binding by ~4-fold (Figure 5B). Interestingly, the enhanced binding was HS dependent, as illustrated by the loss of binding of S protein after HSase treatment (Figure 5B). CRISPR-Cas9-mediated deletion of the *B4GALT7* gene, which is required for glycosaminoglycan assembly (Figure S5B), also reduced binding of S protein (Figure 5B) despite the overexpression of ACE2 (Figure 5A). To explore the impact of diminished ACE2 expression, we examined S protein binding to A549 cells and in two CRISPR-Cas9 gene-targeted clones, C3 and C6, bearing biallelic mutations in ACE2 (Figure S5C). Binding of S ectodomain protein was greatly reduced in the *ACE2*$^{-/-}$ clones, and the residual binding was sensitive to HSases (Figure 5C). These findings show that binding of S protein on cells requires both HS and ACE2, consistent with the formation of a ternary complex (Figures 2F–2H).

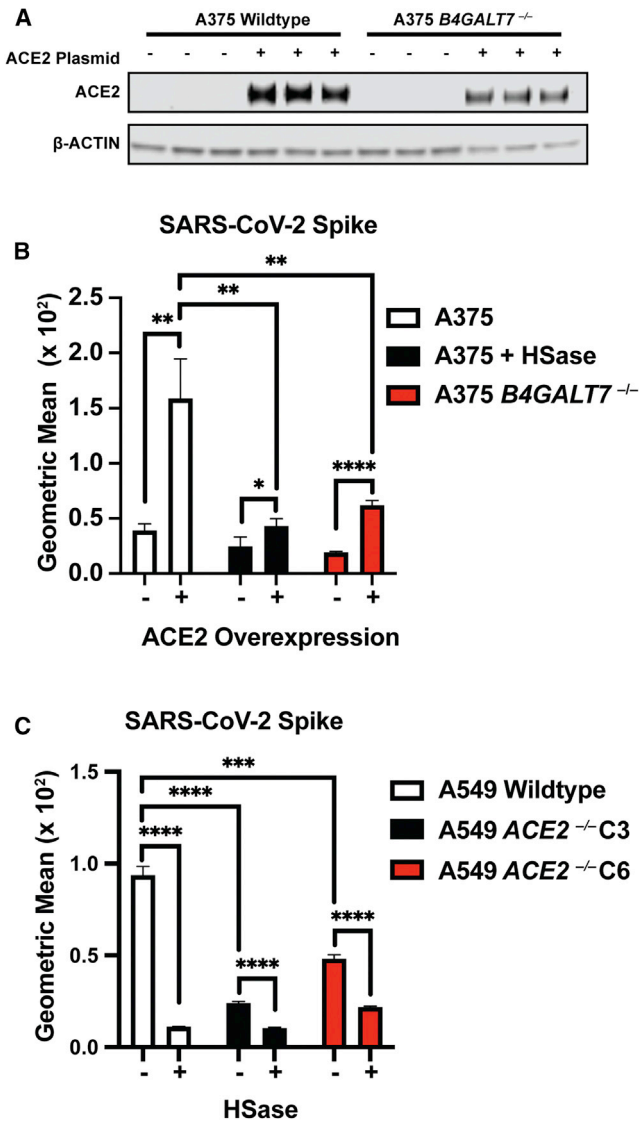

Figure 5. ACE2 and Cellular Heparan Sulfate Are Both Necessary for Binding of SARS-CoV-2 Spike Ectodomain

(A) Western blot shows overexpression of ACE2 in the A375 and A375 *B4GALT7*$^{-/-}$ cells. A representative blot is shown.

(B) Binding of SARS-CoV-2 spike protein to cells with and without ACE2 overexpression. Note that binding is reduced in the cells deficient in HS.

(C) Gene targeting of ACE2 in A549 using CRISPR-Cas9. The bars show spike binding to two independent ACE2 CRISPR-Cas9 knockout clones with and without HSase treatment. Note that binding depends on ACE2 expression and that residual binding depends in part on HS. All analyses were done by flow cytometry. The graphs show representative experiments performed in triplicate technical replicates. Statistical analysis by unpaired t test. (ns: $p > 0.05$, *: $p \leq 0.05$, **: $p \leq 0.01$, ***: $p \leq 0.001$, ****: $p \leq 0.0001$).

See also Figure S5.

Vesicular Stomatitis Virus Spike Protein Pseudotyped Virus Infection Depends on Heparan Sulfate

Assays using purified components provide biochemical insights into binding, but they do not recapitulate the multivalent presentation of the S protein as it occurs on the virion membrane. Thus,

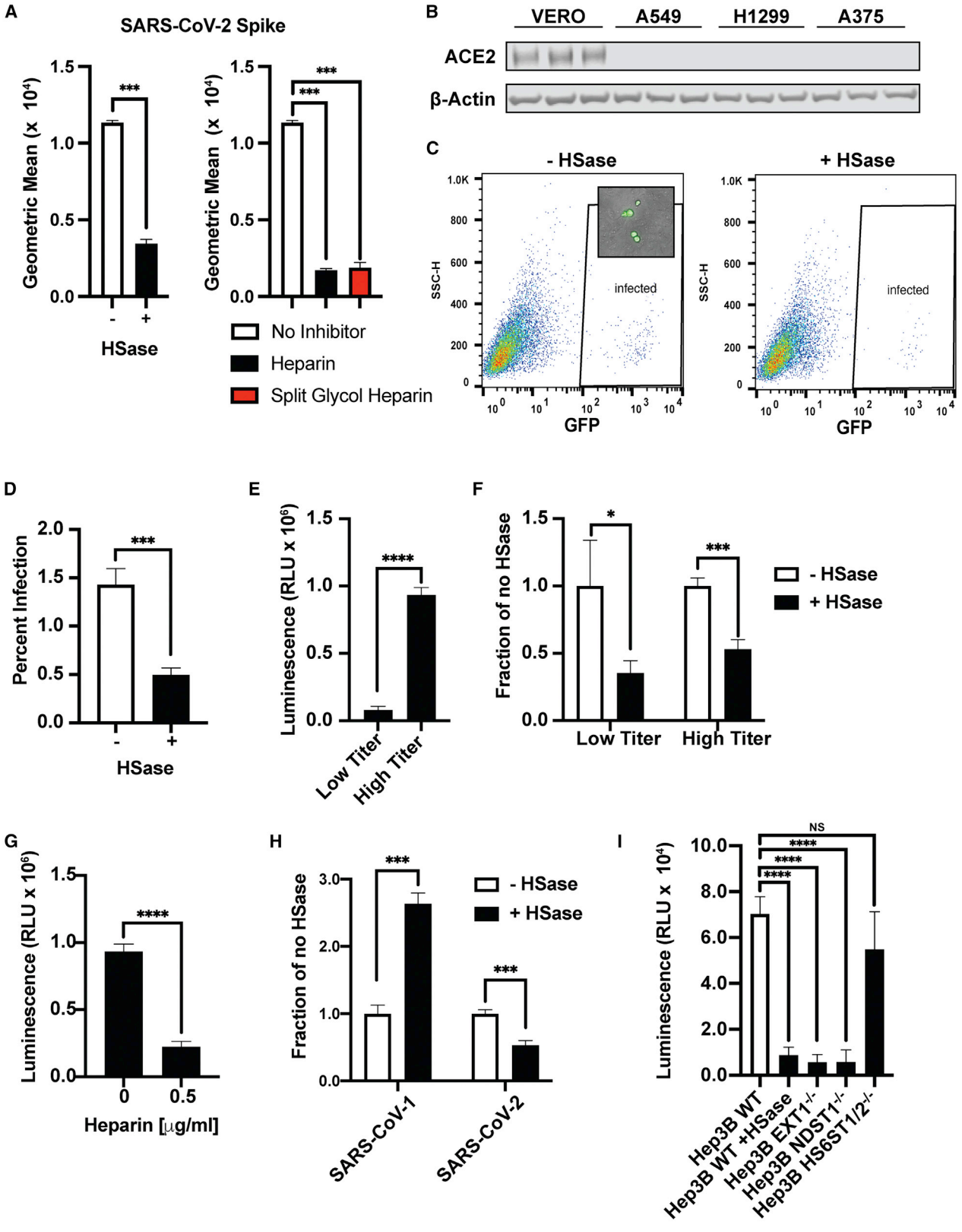

(legend on next page)

to extend these studies, pseudotyped vesicular stomatitis virus (VSV) was engineered to express the full-length SARS-CoV-2 S protein and GFP or luciferase to monitor infection. Vero E6 cells are commonly used in the study of SARS-CoV-2 infection due to their high susceptibility to infection. S protein binding to Vero cells also depends on cellular HS, as binding was sensitive to HSases, heparin, and split-glycol heparin (Figure 6A). Interestingly, HSase treatment reduced binding to a lesser extent than the level of reduction observed in A549, H1299, and Hep3B cells (Figure 3). The decrease in sensitivity to HSase may be due to the very high levels of ACE2 expression in comparison to other cells (western blotting, Figure 6B; qRT-PCR, Figure S5A).

Infection of Vero cells by GFP-expressing VSV S protein pseudotyped virus was readily assessed qualitatively by fluorescence microscopy (inset) and quantitatively by flow cytometry (Figures 6C and 6D). HSase treatment reduced infection ~3-fold. Infection by luciferase-expressing VSV S protein pseudotyped virus provided greater sensitivity, allowing studies with both high and low infection rates (Figures 6E and 6F). Under either condition, infection was reduced 2- to 3-fold by HSase. Heparin very potently reduced infection more than ~4-fold at 0.5 μg/mL and higher concentrations (Figure 6G). In contrast, studies of SARS-CoV-1 S protein pseudotyped virus showed that HSase-treatment actually increased SARS-CoV-1 infection by more than 2-fold, suggesting that HS might interfere with binding of SARS-CoV-1 in this cell line (Figure 6H). Infection of H1299 and A549 cells by SARS-CoV-2 S pseudotyped virus was too low to obtain accurate measurements, but infection of Hep3B cells could be readily measured (Figure 6I). HSase and mutations in *EXT1* and *NDST1* dramatically reduced infection 6- to 7-fold. Inactivation of the 6-*O*-sulfotransferases had only a mild effect unlike its strong effect on S protein binding (Figure 3F), possibly due to the high valency conferred by multiple copies of S protein on the pseudovirus envelope. Hep3B cells were not susceptible to infection by SARS-CoV-1 S protein pseudotyped virus but was infected by MERS-CoV S protein pseudotyped virus, and infection was independent of HS (Figure S6).

Cellular Heparan Sulfate Is Required for Efficient Infection by Authentic SARS-CoV-2 Virus

Studies of pseudovirus were then extended to authentic SARS-CoV-2 virus infection using strain USA-WA1/2020. Infection of Vero E6 cells was monitored by double staining of the cells with antibodies against the SARS-CoV-2 nucleocapsid (N) and S proteins (Figure 7A). Cells were treated with virus for 1 h and the extent of infection was assayed one day later. Varying the MOI (0.2–0.5) yielded infection rates that ranged from 15%–50%. Treatment of the cells with HSases caused, on average, a ~5-fold reduction in the percentage of infected cells. Composite data from five separate experiments done in triplicate are shown in Figure 7B (color coded for individual experiments). Data normalized to the values obtained in the absence of any treatment (mock) is shown in Figure 7C. Titration of UFH showed dose-dependent inhibition of infection (Figures 7B and 7C), with cells infected at a lower MOI showing greater sensitivity to heparin inhibition (maroon and blue symbols). To rule out that the treatments caused a decrease in ACE2 expression or a reduction in cell viability, Vero cells were treated with heparin lyases and 100 μg/mL UFH, and ACE2 expression was measured by western blotting and cell viability by CellTiter-Blue (Figures S7A and S7B). No effect on ACE2 expression or cell viability was observed. These findings further emphasize the potential for using UFH or other non-anticoagulant heparinoids to prevent viral attachment.

These findings were then extended to Hep3B cells and mutants altered in HS biosynthesis using a viral plaque assay. Virus was added to wild-type, *NDST1*$^{-/-}$, and *HS6ST1/2*$^{-/-}$ cells for 2 h, the virus was removed, and after 2 days incubation, a serial dilution of the conditioned culture medium was added to monolayers of Vero E6 cells. The number of plaques was then quantitated by staining and visualization. As a control, culture medium from infected Vero E6 cells was tested, which showed robust viral titers. Hep3B cells also supported viral replication, but to a lesser extent than Vero cells. Inactivation of *NDST1* in Hep3B cells abolished virus production, whereas inactivation of *HS6ST1/2*$^{-/-}$ reduced infection more mildly, ~3-fold (Figure 7D).

Finally, to explore the role of cellular HS in SARS-CoV-2 infection of primary human bronchial epithelial cells, cells were grown at an air-liquid interface and infected with authentic SARS-CoV-2 virus with and without prior HSase treatment or addition of UFH. Infection was assessed by flow cytometry using antibodies against the viral N protein

Figure 6. SARS-CoV-2 Pseudovirus Infection Depends on Heparan Sulfate

(A) Left, SARS-CoV-2 spike protein (20 μg/mL) binding to Vero cells measured by flow cytometry with and without HSase. Right, heparin and split-glycol heparin inhibit SARS-CoV-2 spike protein (20 μg/mL) binding to Vero cells by flow cytometry. Statistical analysis by unpaired t test.

(B) Western blot analysis of ACE2 expression in Vero E6 cells compared to A549, H1299, and A375 cells. A representative blot of three extracts is shown for each strain.

(C) Infection of Vero E6 cells with SARS-CoV-2 spike protein expressing pseudotyped virus expressing GFP. Infection was done with and without HSase treatment of the cells. Insert shows GFP expression in the infected cells by imaging. Counting was performed by flow cytometry with gating for GFP-positive cells as indicated by "infected."

(D) Quantitative analysis of GFP-positive cells.

(E) Infection of Vero E6 cells with SARS-CoV-2 S protein pseudotyped virus expressing luciferase, as measured by the addition of Bright-Glo and detection of luminescence. The figure shows infection experiments done at low and high titer.

(F) HSase treatment diminishes infection by SARS-CoV-2 S protein pseudotyped virus (luciferase) at low and high titer.

(G) Heparin (0.5 μg/mL) blocks infection with SARS-CoV-2 S protein pseudotyped virus (luciferase).

(H) Effect of HSase treatment of Vero E6 cells on the infection of both SARS-CoV-1 S and SARS-CoV-2 S protein pseudotyped virus expressing luciferase.

(I) Infection of Hep3B with and without HSase and in Hep3B cells containing mutations in *EXT1*, *NDST1*, and *HS6ST1*/*HS6ST2*. Cells were infected with SARS-CoV-2 S protein pseudotyped virus expressing luciferase. All experiments were repeated at least three times. Graphs shows representative experiments performed in technical triplicates. Statistical analysis by unpaired t test. (ns: $p > 0.05$, *$p \leq 0.05$, **$p \leq 0.01$, ***$p \leq 0.001$, ****$p \leq 0.0001$).

See also Figure S6.

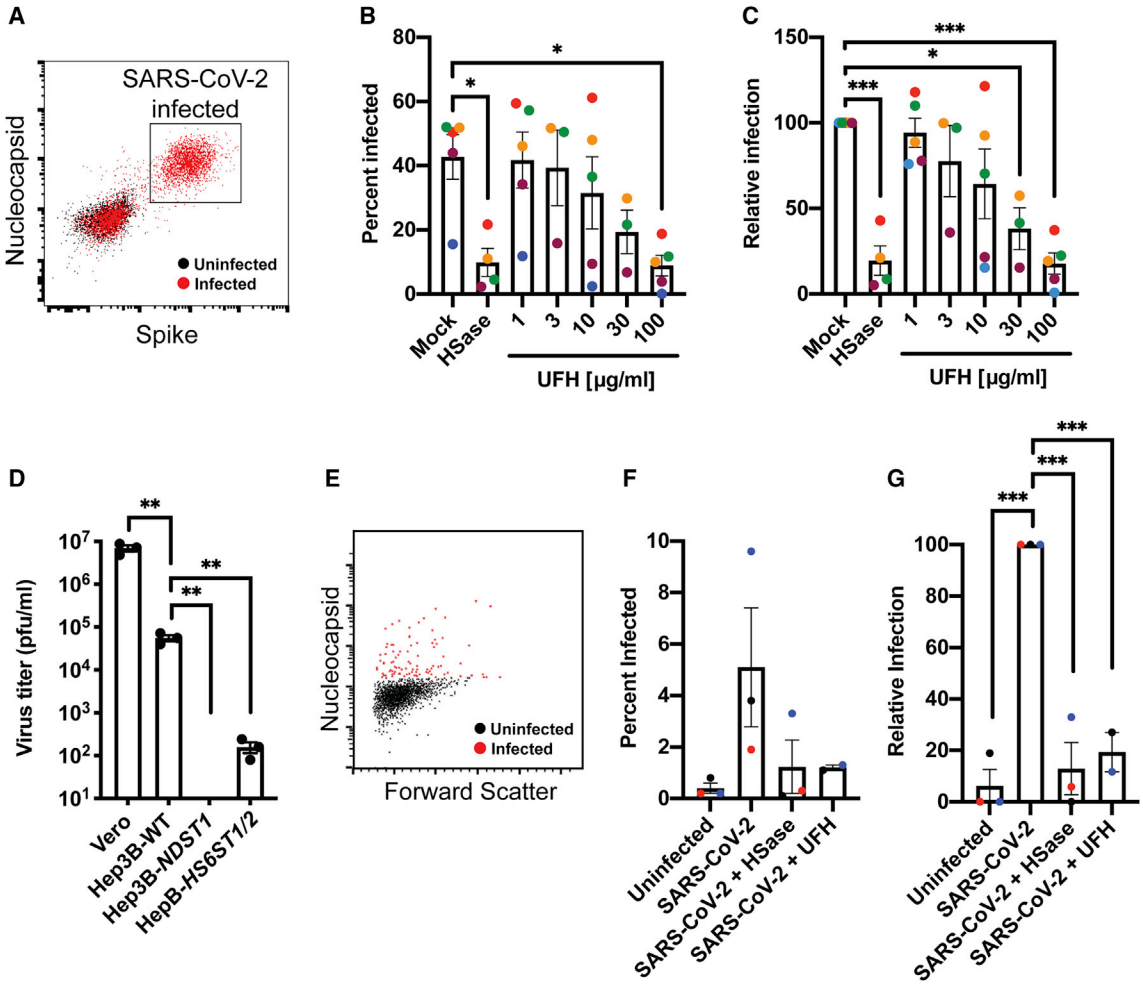

Figure 7. Manipulation of Cellular Heparan Sulfate Decreases Infection of Authentic SARS-CoV-2 Virus

(A,) Flow cytometry analysis of SARS-CoV-2-infected (red) or uninfected (black) Vero cells stained with antibodies against SARS-CoV-2 nucleocapsid and spike protein.

(B) SARS-CoV-2 infection of Vero cells performed in the absence and presence of HSase, or with incubation with different concentrations of unfractionated heparin (UFH). The extent of infection was analyzed by flow cytometry as in (A). The graph shows a composite of five separate experiments, each performed in triplicate. The MOI was 0.5, but the extent of infection varied. The MOI in the experiment shown in maroon and blue was 0.2. The mean data from the individual experiments are colorized to allow for separate visualization

(C) Same data as in (B), but with the experimental data normalized to the mock infection for each respective experiment.

(D) SARS-CoV-2 infection of Hep3B mutants altered in HS biosynthesis enzymes. Cells were infected for 1 h and incubated 48 h, allowing for new virus to form. The resulting viral titers in the culture supernatants were determined by plaque assays on Vero E6 cells. Average values with standard error mean are shown, along with the individual data points. The experiment was initially optimized and then performed in triplicate.

(E) Flow cytometry analysis of SARS-CoV-2-infected (red) or uninfected (black) human bronchial epithelial cells at an air-liquid interface stained with antibodies against SARS-CoV-2 nucleocapsid.

(F) SARS-CoV-2 infection of human bronchial epithelial cells at an air-liquid interface was performed in the absence and presence of HSase, or with incubation UFH. The extent of infection was analyzed by flow cytometry. The graph shows a composite of three separate experiments, each performed in triplicate. The mean data from the individual experiments are colorized to allow for separate visualization.

(G) Same data as in (F), but with each experimental dataset normalized to the uninfected control. Statistical analysis by one-way ANOVA (B, C, and G) or unpaired t test (D); ns: $p > 0.05$, *: $p \leq 0.05$, **: $p \leq 0.01$, ***: $p \leq 0.001$, ****: $p \leq 0.0001$).

See also Figure S7.

(Figure 7E). Composite data from three separate experiments each done in triplicate are shown in Figure 7F (again color coded for individual experiments). Data normalized to the values obtained in the absence of any treatment (uninfected) is shown in Figure 7G. Treatment with HSase and UFH reduced infection more than 5-fold, but it had no effect on cell viability (Figure S7C). These findings demonstrate the requirement of cellular HS in mediating infection of authentic human bronchial epithelial cells by SARS-CoV-2.

DISCUSSION

In this report, we provide compelling evidence that HS is a necessary host attachment factor that promotes SARS-CoV-2 infection of various target cells. The RBD of the SARS-CoV-2 S protein binds to heparin/HS, most likely through a docking site composed of positively charged amino acid residues aligned in a subdomain of the RBD that is separate from the site involved in ACE2 binding (Figure 1). Competition studies, enzymatic removal of HS, and genetic studies confirm that the S protein, whether presented as a recombinant protein (Figures 2, 3, 4, and 5) in a pseudovirus (Figure 6) or in authentic SARS-CoV-2 virions (Figure 7), binds to cell surface HS in a cooperative manner with ACE2 receptors. Mechanistically, binding of heparin/HS to S trimers enhances binding to ACE2, likely increasing multivalent interactions with the target cell. These data provide crucial insights into the pathogenic mechanism of SARS-CoV-2 infection and suggest HS-S protein complexes as a novel therapeutic target to prevent infection.

The glycocalyx is the first point of contact for all pathogens that infect animal cells, and thus it is not surprising that many viruses exploit glycans, such as HS, as attachment factors. For example, the initial interaction of herpes simplex virus with cells involves binding to HS chains on one or more HS proteoglycans (Shieh et al., 1992; WuDunn and Spear, 1989) through the interactions with the viral glycoproteins gB and gC. Viral entry requires the interaction of a specific structure in HS with a third viral glycoprotein, gD (Shukla et al., 1999), working in concert with membrane proteins related to TNF/NGF receptors (Montgomery et al., 1996). Similarly, the human immunodeficiency virus binds to HS by way of the V3 loop of the viral glycoprotein gp120 (Roderiquez et al., 1995), but infection requires the chemokine receptor CCR5 (Deng et al., 1996; Dragic et al., 1996). Other coronaviruses also utilize HS; for example, NL63 (HCoV-NL63) binds HS via the viral S protein in addition to ACE2 (Lang et al., 2011; Milewska et al., 2014, 2018; Naskalska et al., 2019). In these examples, initial tethering of virions to the host cell plasma membrane appears to be mediated by HS, but infection requires transfer to a proteinaceous receptor. The data presented here show that SARS-CoV-2 requires HS in addition to ACE2. We imagine a model in which cell surface HS acts as a ''collector'' of the virus and a mediator of the RBD-ACE2 interaction, making viral infection more efficient. HS varies in structure across cell types and tissues, as well as with gender and age (de Agostini et al., 2008; Feyzi et al., 1998; Ledin et al., 2004; Vongchan et al., 2005; Warda et al., 2006; Wei et al., 2011). Variation in competition by HS from different tissues supports this conclusion and raises the possibility that HS contributes to the tissue tropism and the susceptibility of different patient populations, in addition to levels of expression of ACE2 (Li et al., 2020).

Coronaviruses can utilize a diverse set of glycoconjugates as attachment factors. Human coronavirus OC43 (HCoV-OC43) and bovine coronavirus (BCoV) bind to 5-*N*-acetyl-9-*O*-acetyl-neuraminic acid (Hulswit et al., 2019; Tortorici et al., 2019), middle east respiratory syndrome virus (MERS-CoV) binds to 5-*N*-acetyl-neuraminic acid (Park et al., 2019), and guinea fowl coronavirus binds biantennary di-*N*-acetyllactosamine or sialic acid-capped glycans (Bouwman et al., 2019). Whether SARS-CoV-2 S protein binds to sialic acid remains unclear. Mapping the binding site for sialic acids in other coronavirus S proteins has proved elusive, but modeling studies suggest a location distinct from the HS-binding site shown in Figure 1 (Park et al., 2019; Tortorici et al., 2019). The S protein in murine coronavirus contains both a hemagglutinin domain for binding and an esterase domain that cleaves sialic acids that aids in the liberation of bound virions (Rinninger et al., 2006; Smits et al., 2005). Whether SARS-CoV-2 S protein, another viral envelope protein, or a host protein contributes to HS-degrading activity to aid in the release of newly made virions is unknown.

The repertoire of proteins in organisms that bind to HS make up the so called ''HS interactome'' and consists of a variety of different HSBPs (Xu and Esko, 2014). Unlike lectins that have a common fold that helps define the glycan-binding site, HSBPs do not exhibit a conserved motif that allows accurate predictions of binding sites based on primary sequence. Instead, the capacity to bind heparin appears to have emerged through convergent evolution by juxtaposition of several positively charged amino acid residues arranged to accommodate the negatively charged sulfate and carboxyl groups present in the polysaccharide, and hydrophobic and H-bonding interactions stabilize the association. The RBDs from the SARS-CoV-1 and SARS-CoV-2 S proteins are highly similar in structure (Figure 1G), but the electropositive surface in the SARS-CoV-1 S RBD is not as pronounced in the SARS-CoV-2 S RBD (Figure 1H). In accordance with this observation, recombinant RBD protein from SARS-CoV-2 showed significantly higher binding to heparin-BSA, compared to RBD from SARS-CoV-1 (Figure 2B). *A priori*, we predicted that the evolution of the HS-binding site in the SARS-CoV-2 S protein might have occurred by the addition of arginine and lysine residues to its ancestor, SARS-CoV-1. Instead, we observed that four of the six predicted positively charged residues that make up the heparin-binding site are present in SARS-CoV-1, as well as most of the other amino acid residues predicted to interact with heparin (Figure 1). SARS-CoV-1 has been shown to interact with cellular HS in addition to its entry receptors ACE2 and transmembrane protease, serine 2 (TMPRSS2) (Lang et al., 2011). Our analysis suggests that the putative heparin-binding site in SARS-CoV-2 S may mediate an enhanced interaction with heparin compared to SARS-CoV-1 and that this change evolved through as few as two amino acid substitutions, Thr444Lys and Glu354Asn. Further studies are underway to define the amino acid residues in the combining site for heparin/HS to test this hypothesis.

The ability of heparin and HS to compete for binding of the SARS-CoV-2 S protein to cell surface HS and the inhibitory activity of heparin toward infection of pseudovirus and authentic SARS-CoV-2 illustrates the therapeutic potential of agents that target the virus-HS interaction to control infection and transmission of SARS-CoV-2. There is precedent for targeting protein-glycan interactions as therapeutic agents. For example, Tamiflu targets influenza neuraminidase, thus reducing viral transmission, and sialylated human milk oligosaccharides can block sialic-acid-dependent rotavirus attachment and subsequent infection in infants (Hester et al., 2013; von Itzstein, 2007). COVID-19 patients typically suffer from thrombotic complications ranging from vascular micro-thromboses, venous

thromboembolic disease, and stroke, and often receive UFH or low molecular weight heparin (Thachil, 2020). The findings presented here and elsewhere suggest that both of these agents can block viral infection (Mycroft-West et al., 2020a, 2020b; Kim et al., 2020; Liu et al., 2020; Tandon et al., 2020; Wu et al., 2020). Effective anticoagulation is achieved with plasma levels of heparin of 0.3–0.7 units/mL. This concentration is equivalent to 1.6–4 μg/mL heparin (assuming the activity of UFH is 180 units/mg). Although this is sufficient to block S protein binding to cells (Figure 4), it would not be expected to prevent viral infection, but it should attenuate infection depending on the viral load (Figure 7). The anticoagulant activity of heparin, which is typically absent in HS, is not critical for its antiviral activity based on the observation that MST-derived heparin and split-glycol heparin are nearly as potent as therapeutic heparin (Figures 4 and 6). Additional studies are needed to address the potential overlap in the dose response profiles for heparin as an anticoagulant and antiviral agent and the utility of non-anticoagulant heparins. Antibodies directed to HS or the binding site in the RBD might also prove useful for attenuating infection.

In conclusion, this work revealed HS as a novel attachment factor for SARS-CoV-2 and suggests the possibility of using HS mimetics, HS degrading lyases, and metabolic inhibitors of HS biosynthesis for the development of therapy to combat COVID-19.

STAR★METHODS

Detailed methods are provided in the online version of this paper and include the following:

- KEY RESOURCES TABLE
- RESOURCE AVAILABILITY
  - Lead Contact
  - Materials Availability
  - Data and Code Availability
- EXPERIMENTAL MODEL AND SUBJECT DETAILS
  - Cell Lines
  - Primary Cell Cultures
  - Human Subjects
- METHOD DETAILS
  - Molecular Modeling
  - SARS-CoV-2 spike protein production
  - SARS-CoV-2 spike RBD production
  - Transmission electron microscopy
  - Recombinant ACE2 expression and purification
  - Analytical Heparin-Sepharose Chromatography
  - Biotinylation
  - Binding of spike protein to heparin
  - Immobilization and binding of ACE2, spike and heparin-BSA
  - Negative stain-electron microscopy to visualize the spike, ACE2, and heparin interaction
  - Flow cytometry
  - HS purification from tissues
  - HS digestion and LC-MS analysis
  - ACE2 overexpression and immunoblotting
  - qPCR
  - Mutant cell line generation
  - Preparation and infection by pseudotyped VSV
  - Infection by authentic SARS-CoV-2 virus
  - Virus plaque assays
  - Human bronchial epithelial cell air-liquid interface generation and infection
  - Cell Viability Assay
- QUANTIFICATION AND STATISTICAL ANALYSIS

ACKNOWLEDGMENTS

We thank Scott Selleck (Pennsylvania State University), Eugene Yeo (UC San Diego), John Guatelli (UC San Diego), Mark Fuster (UC San Diego), and Stephen Schoenberger (La Jolla Institute for Immunology) for many helpful discussions, and Annamaria Naggi and Giangiacomo Torri from the Ronzoni Institute for generously providing split-glycol heparin. This work was supported by RAPID grant 2031989 from the National Science Foundation and Project 3 of NIH P01 HL131474 to J.D.E., the Alfred Benzon Foundation to T.M. Clausen, NIH R01 AI146779 and a Massachusetts Consortium on Pathogen Readiness (MassCPR) grant to A.G.S., DOD grant W81XWH-20-1-0270 and Fluomics/NOSI U19 AI135972 to S.K.C., a Career Award for Medical Scientists from the Burroughs Wellcome Fund to A.F.C., Bill and Melinda Gates Foundation grant OPP1170236 to A.B.W., COVID-19 seed funding from the Huck Institutes of the Life Sciences and Penn State start-up funds to J.J., funding for Z.Y. from grant DNRF107 from the Danish National Research Foundation, and T32 training grants GM007753 to B.M.H. and T.M. Caradonna and AI007245 for J.F. J.P. received funding from Innovation Fund Denmark and VAR2 Pharmaceuticals.

AUTHOR CONTRIBUTIONS

T.M. Clausen, D.R.S., and J.D.E. conceived, initiated, and coordinated the project. T.M. Clausen, D.R.S., C.B.S., J.P., H.R.P., C.D.P., A.N., S.A.M., E.M.K., R.N.M., J.L.T., B.E.T., C.A.G., G.J.G., A.F.G., S.L.L., and A.F.C. designed and performed the experimental work. Z.Y., R.N.P., L.L., J.F., X.Y., Y.P., B.M.H., T.M. Caradonna, S.K.C., K.G., A.B.W., A.G.S., and K.G. supplied reagents. P.L.B., B.P.K., C.M., J.J., K.D.C., and P.L.S.M.G. provided essential discussion and advice. T.M. Clausen, D.R.S., and J.D.E. performed the main fundraising. T.M. Clausen, D.R.S., and J.D.E. wrote the manuscript. All authors discussed the experiments and results and read and approved the manuscript.

DECLARATION OF INTERESTS

J.D.E. is a co-founder of TEGA Therapeutics. J.D.E. and the Regents of the University of California have licensed a University invention to and have an equity interest in TEGA Therapeutics. The terms of this arrangement have been reviewed and approved by the University of California, San Diego in accordance with its conflict of interest policies. C.A.G. and B.E.T. are employees of TEGA Therapeutics.

Received: July 13, 2020
Revised: August 16, 2020
Accepted: September 10, 2020
Published: September 14, 2020

REFERENCES

Anower-E-Khuda, F., Singh, G., Deng, Y., Gordts, P.L.S.M., and Esko, J.D. (2019). Triglyceride-rich lipoprotein binding and uptake by heparan sulfate proteoglycan receptors in a CRISPR/Cas9 library of Hep3B mutants. Glycobiology *29*, 582–592.

Beigel, J.H., Tomashek, K.M., Dodd, L.E., Mehta, A.K., Zingman, B.S., Kalil, A.C., Hohmann, E., Chu, H.Y., Luetkemeyer, A., Kline, S., et al. (2020).

Remdesivir for the Treatment of Covid-19 - Preliminary Report. N Engl J Med *NEJMoa2007764*. https://doi.org/10.1056/NEJMoa2007764.

Bouwman, K.M., Delpont, M., Broszeit, F., Berger, R., Weerts, E.A.W.S., Lucas, M.N., Delverdier, M., Belkasmi, S., Papanikolaou, A., Boons, G.J., et al. (2019). Guinea Fowl Coronavirus Diversity Has Phenotypic Consequences for Glycan and Tissue Binding. J. Virol. *93* https://doi.org/10.1128/JVI.00067-19.

Cagno, V., Tseligka, E.D., Jones, S.T., and Tapparel, C. (2019). Heparan Sulfate Proteoglycans and Viral Attachment: True Receptors or Adaptation Bias? Viruses *11*. https://doi.org/10.3390/v11070596.

Casu, B., Guerrini, M., Guglieri, S., Naggi, A., Perez, M., Torri, G., Cassinelli, G., Ribatti, D., Carminati, P., Giannini, G., et al. (2004). Undersulfated and glycol-split heparins endowed with antiangiogenic activity. J. Med. Chem. *47*, 838–848.

de Agostini, A.I., Dong, J.C., de Vantéry Arrighi, C., Ramus, M.A., Dentand-Quadri, I., Thalmann, S., Ventura, P., Ibecheole, V., Monge, F., Fischer, A.M., et al. (2008). Human follicular fluid heparan sulfate contains abundant 3-O-sulfated chains with anticoagulant activity. J. Biol. Chem. *283*, 28115–28124.

Deng, H., Liu, R., Ellmeier, W., Choe, S., Unutmaz, D., Burkhart, M., Di Marzio, P., Marmon, S., Sutton, R.E., Hill, C.M., et al. (1996). Identification of a major co-receptor for primary isolates of HIV-1. Nature *381*, 661–666.

Dragic, T., Litwin, V., Allaway, G.P., Martin, S.R., Huang, Y., Nagashima, K.A., Cayanan, C., Maddon, P.J., Koup, R.A., Moore, J.P., and Paxton, W.A. (1996). HIV-1 entry into CD4+ cells is mediated by the chemokine receptor CC-CKR-5. Nature *381*, 667–673.

Esko, J.D., Ausubel, F., Brent, R., Kingston, B., Moore, D., Seidman, J., Smith, J., Struhl, K., Varki, A., and Coligan, J. (1993). Special considerations for proteoglycans and glycosaminoglycans and their purification. Current protocols in molecular biology (New York: Greene Publishing and Wiley-Interscience), pp. 17.12.11–17.12.19.

Esko, J.D., and Selleck, S.B. (2002). Order out of chaos: assembly of ligand binding sites in heparan sulfate. Annu. Rev. Biochem. *71*, 435–471.

Feyzi, E., Saldeen, T., Larsson, E., Lindahl, U., and Salmivirta, M. (1998). Age-dependent modulation of heparan sulfate structure and function. J. Biol. Chem. *273*, 13395–13398.

Gasimli, L., Glass, C.A., Datta, P., Yang, B., Li, G., Gemmill, T.R., Baik, J.Y., Sharfstein, S.T., Esko, J.D., and Linhardt, R.J. (2014). Bioengineering murine mastocytoma cells to produce anticoagulant heparin. Glycobiology *24*, 272–280.

Goddard, T.D., Huang, C.C., Meng, E.C., Pettersen, E.F., Couch, G.S., Morris, J.H., and Ferrin, T.E. (2018). UCSF ChimeraX: Meeting modern challenges in visualization and analysis. Protein Sci. *27*, 14–25.

Han, X., Sanderson, P., Nesheiwat, S., Lin, L., Yu, Y., Zhang, F., Amster, I.J., and Linhardt, R.J. (2020). Structural analysis of urinary glycosaminoglycans from healthy human subjects. Glycobiology *30*, 143–151.

Hester, S.N., Chen, X., Li, M., Monaco, M.H., Comstock, S.S., Kuhlenschmidt, T.B., Kuhlenschmidt, M.S., and Donovan, S.M. (2013). Human milk oligosaccharides inhibit rotavirus infectivity in vitro and in acutely infected piglets. Br. J. Nutr. *110*, 1233–1242.

Hulswit, R.J.G., Lang, Y., Bakkers, M.J.G., Li, W., Li, Z., Schouten, A., Ophorst, B., van Kuppeveld, F.J.M., Boons, G.J., Bosch, B.J., et al. (2019). Human coronaviruses OC43 and HKU1 bind to 9-*O*-acetylated sialic acids via a conserved receptor-binding site in spike protein domain A. Proc. Natl. Acad. Sci. USA *116*, 2681–2690.

Kaneko, N., Kuo, H.H., Boucau, J., Farmer, J.R., Allard-Chamard, H., Mahajan, V.S., Piechocka-Trocha, A., Lefteri, K., Osborn, M., Bals, J., et al. (2020). Loss of Bcl-6-Expressing T Follicular Helper Cells and Germinal Centers in COVID-19. Cell. https://doi.org/10.1016/j.cell.2020.08.025.

Kim, S.Y., Jin, W., Sood, A., Montgomery, D.W., Grant, O.C., Fuster, M.M., Fu, L., Dordick, J.S., Woods, R.J., Zhang, F., et al. (2020). Glycosaminoglycan binding motif at S1/S2 proteolytic cleavage site on spike glycoprotein may facilitate novel coronavirus (SARS-CoV-2) host cell entry. bioRxiv. https://doi.org/10.1101/2020.04.14.041459.

Kirchdoerfer, R.N., Wang, N., Pallesen, J., Wrapp, D., Turner, H.L., Cottrell, C.A., Corbett, K.S., Graham, B.S., McLellan, J.S., and Ward, A.B. (2018). Stabilized coronavirus spikes are resistant to conformational changes induced by receptor recognition or proteolysis. Sci. Rep. *8*, 15701.

Koehler, M., Delguste, M., Sieben, C., Gillet, L., and Alsteens, D. (2020). Initial Step of Virus Entry: Virion Binding to Cell-Surface Glycans. Annu. Rev. Virol. *7* https://doi.org/10.1146/annurev-virology-122019-070025.

Kozakov, D., Beglov, D., Bohnuud, T., Mottarella, S.E., Xia, B., Hall, D.R., and Vajda, S. (2013). How good is automated protein docking? Proteins *81*, 2159–2166.

Kozakov, D., Hall, D.R., Xia, B., Porter, K.A., Padhorny, D., Yueh, C., Beglov, D., and Vajda, S. (2017). The ClusPro web server for protein-protein docking. Nat. Protoc. *12*, 255–278.

Lander, G.C., Stagg, S.M., Voss, N.R., Cheng, A., Fellmann, D., Pulokas, J., Yoshioka, C., Irving, C., Mulder, A., Lau, P.W., et al. (2009). Appion: an integrated, database-driven pipeline to facilitate EM image processing. J. Struct. Biol. *166*, 95–102.

Lang, J., Yang, N., Deng, J., Liu, K., Yang, P., Zhang, G., and Jiang, C. (2011). Inhibition of SARS pseudovirus cell entry by lactoferrin binding to heparan sulfate proteoglycans. PLoS ONE *6*, e23710.

Lawrence, R., Olson, S.K., Steele, R.E., Wang, L., Warrior, R., Cummings, R.D., and Esko, J.D. (2008). Evolutionary differences in glycosaminoglycan fine structure detected by quantitative glycan reductive isotope labeling. J. Biol. Chem. *283*, 33674–33684.

Ledin, J., Staatz, W., Li, J.P., Götte, M., Selleck, S., Kjellén, L., and Spillmann, D. (2004). Heparan sulfate structure in mice with genetically modified heparan sulfate production. J. Biol. Chem. *279*, 42732–42741.

Li, W., Moore, M.J., Vasilieva, N., Sui, J., Wong, S.K., Berne, M.A., Somasundaran, M., Sullivan, J.L., Luzuriaga, K., Greenough, T.C., et al. (2003). Angiotensin-converting enzyme 2 is a functional receptor for the SARS coronavirus. Nature *426*, 450–454.

Li, G., He, X., Zhang, L., Ran, Q., Wang, J., Xiong, A., Wu, D., Chen, F., Sun, J., and Chang, C. (2020). Assessing ACE2 expression patterns in lung tissues in the pathogenesis of COVID-19. J. Autoimmun. *112*, 102463.

Lindahl, U., Couchman, J., Kimata, K., and Esko, J.D. (2015). Proteoglycans and Sulfated Glycosaminoglycans. In Essentials of Glycobiology, A. Varki, R.D. Cummings, J.D. Esko, P. Stanley, G.W. Hart, M. Aebi, A.G. Darvill, T. Kinoshita, N.H. Packer, and J.H. Prestegard, et al., eds. (Cold Spring Harbor, NY: Cold Spring Harbor Laboratory Press), pp. 207–221.

Liu, L., Chopra, P., Li, X., Wolfert, M.A., Tompkins, S.M., and Boons, G.J. (2020). SARS-CoV-2 spike protein binds heparan sulfate in a length- and sequence-dependent manner. bioRxiv. https://doi.org/10.1101/2020.05.10.087288.

Milewska, A., Zarebski, M., Nowak, P., Stozek, K., Potempa, J., and Pyrc, K. (2014). Human coronavirus NL63 utilizes heparan sulfate proteoglycans for attachment to target cells. J. Virol. *88*, 13221–13230.

Milewska, A., Nowak, P., Owczarek, K., Szczepanski, A., Zarebski, M., Hoang, A., Berniak, K., Wojarski, J., Zeglen, S., Baster, Z., et al. (2018). Entry of Human Coronavirus NL63 into the Cell. J. Virol. *92* https://doi.org/10.1128/JVI.01933-17.

Montgomery, R.I., Lidholt, K., Flay, N.W., Liang, J., Vertel, B., Lindahl, U., and Esko, J.D. (1992). Stable heparin-producing cell lines derived from the Furth murine mastocytoma. Proc. Natl. Acad. Sci. USA *89*, 11327–11331.

Montgomery, R.I., Warner, M.S., Lum, B.J., and Spear, P.G. (1996). Herpes simplex virus-1 entry into cells mediated by a novel member of the TNF/NGF receptor family. Cell *87*, 427–436.

Mycroft-West, C., Su, D., Elli, S., Guimond, S., Miller, G., Turnbull, J., Yates, E., Guerrini, M., Fernig, D., Lima, M., and Skidmore, M. (2020a). The 2019 coronavirus (SARS-CoV-2) surface protein (Spike) S1 Receptor Binding Domain undergoes conformational change upon heparin binding. BioRxiv. https://doi.org/10.1101/2020.02.29.971093.

Mycroft-West, C.J., Su, D., Pagani, I., Rudd, T.R., Elli, S., Guimond, S.E., Miller, G., Meneghetti, M.C.Z., Nader, H.B., Li, Y., et al. (2020b). Heparin inhibits cellular invasion by SARS-CoV-2: structural dependence of the interaction of the surface protein (spike) S1 receptor binding domain with heparin. bioRxiv. https://doi.org/10.1101/2020.04.28.066761.

Naskalska, A., Dabrowska, A., Szczepanski, A., Milewska, A., Jasik, K.P., and Pyrc, K. (2019). Membrane Protein of Human Coronavirus NL63 Is Responsible for Interaction with the Adhesion Receptor. J. Virol. *93* https://doi.org/10.1128/JVI.00355-19.

Park, Y.J., Walls, A.C., Wang, Z., Sauer, M.M., Li, W., Tortorici, M.A., Bosch, B.J., DiMaio, F., and Veesler, D. (2019). Structures of MERS-CoV spike glycoprotein in complex with sialoside attachment receptors. Nat. Struct. Mol. Biol. *26*, 1151–1157.

Rinninger, A., Richet, C., Pons, A., Kohla, G., Schauer, R., Bauer, H.C., Zanetta, J.P., and Vlasak, R. (2006). Localisation and distribution of O-acetylated N-acetylneuraminic acids, the endogenous substrates of the hemagglutinin-esterases of murine coronaviruses, in mouse tissue. Glycoconj. J. *23*, 73–84.

Roderiquez, G., Oravecz, T., Yanagishita, M., Bou-Habib, D.C., Mostowski, H., and Norcross, M.A. (1995). Mediation of human immunodeficiency virus type 1 binding by interaction of cell surface heparan sulfate proteoglycans with the V3 region of envelope gp120-gp41. J. Virol. *69*, 2233–2239.

Sanjana, N.E., Shalem, O., and Zhang, F. (2014). Improved vectors and genome-wide libraries for CRISPR screening. Nat. Methods *11*, 783–784.

Scheres, S.H. (2012). RELION: implementation of a Bayesian approach to cryo-EM structure determination. J. Struct. Biol. *180*, 519–530.

Shieh, M.-T., WuDunn, D., Montgomery, R.I., Esko, J.D., and Spear, P.G. (1992). Cell surface receptors for herpes simplex virus are heparan sulfate proteoglycans. J. Cell Biol. *116*, 1273–1281.

Shukla, D., Liu, J., Blaiklock, P., Shworak, N.W., Bai, X., Esko, J.D., Cohen, G.H., Eisenberg, R.J., Rosenberg, R.D., and Spear, P.G. (1999). A novel role for 3-*O*-sulfated heparan sulfate in herpes simplex virus 1 entry. Cell *99*, 13–22.

Smits, S.L., Gerwig, G.J., van Vliet, A.L., Lissenberg, A., Briza, P., Kamerling, J.P., Vlasak, R., and de Groot, R.J. (2005). Nidovirus sialate-O-acetylesterases: evolution and substrate specificity of coronaviral and toroviral receptor-destroying enzymes. J. Biol. Chem. *280*, 6933–6941.

Stencel-Baerenwald, J.E., Reiss, K., Reiter, D.M., Stehle, T., and Dermody, T.S. (2014). The sweet spot: defining virus-sialic acid interactions. Nat. Rev. Microbiol. *12*, 739–749.

Suloway, C., Pulokas, J., Fellmann, D., Cheng, A., Guerra, F., Quispe, J., Stagg, S., Potter, C.S., and Carragher, B. (2005). Automated molecular microscopy: the new Leginon system. J. Struct. Biol. *151*, 41–60.

Tandon, R., Sharp, J.S., Zhang, F., Pomin, V.H., Ashpole, N.M., Mitra, D., Jin, W., Liu, H., Sharma, P., and Linhardt, R.J. (2020). Effective Inhibition of SARS-CoV-2 Entry by Heparin and Enoxaparin Derivatives. bioRxiv. https://doi.org/10.1101/2020.06.08.140236.

Thachil, J. (2020). The versatile heparin in COVID-19. J. Thromb. Haemost. *18*, 1020–1022.

Tortorici, M.A., Walls, A.C., Lang, Y., Wang, C., Li, Z., Koerhuis, D., Boons, G.J., Bosch, B.J., Rey, F.A., de Groot, R.J., and Veesler, D. (2019). Structural basis for human coronavirus attachment to sialic acid receptors. Nat. Struct. Mol. Biol. *26*, 481–489.

Vajda, S., Yueh, C., Beglov, D., Bohnuud, T., Mottarella, S.E., Xia, B., Hall, D.R., and Kozakov, D. (2017). New additions to the ClusPro server motivated by CAPRI. Proteins *85*, 435–444.

von Itzstein, M. (2007). The war against influenza: discovery and development of sialidase inhibitors. Nat. Rev. Drug Discov. *6*, 967–974.

Vongchan, P., Warda, M., Toyoda, H., Toida, T., Marks, R.M., and Linhardt, R.J. (2005). Structural characterization of human liver heparan sulfate. Biochim. Biophys. Acta *1721*, 1–8.

Voss, N.R., Yoshioka, C.K., Radermacher, M., Potter, C.S., and Carragher, B. (2009). DoG Picker and TiltPicker: software tools to facilitate particle selection in single particle electron microscopy. J. Struct. Biol. *166*, 205–213.

Walls, A.C., Park, Y.J., Tortorici, M.A., Wall, A., McGuire, A.T., and Veesler, D. (2020). Structure, Function, and Antigenicity of the SARS-CoV-2 Spike Glycoprotein. Cell *181*, 281–292.e6.

Warda, M., Toida, T., Zhang, F., Sun, P., Munoz, E., Xie, J., and Linhardt, R.J. (2006). Isolation and characterization of heparan sulfate from various murine tissues. Glycoconj. J. *23*, 555–563.

Watanabe, Y., Allen, J.D., Wrapp, D., McLellan, J.S., and Crispin, M. (2020). Site-specific glycan analysis of the SARS-CoV-2 spike. Science *369*, 330–333.

Wei, W., Niñonuevo, M.R., Sharma, A., Danan-Leon, L.M., and Leary, J.A. (2011). A comprehensive compositional analysis of heparin/heparan sulfate-derived disaccharides from human serum. Anal. Chem. *83*, 3703–3708.

Whitt, M.A. (2010). Generation of VSV pseudotypes using recombinant ΔG-VSV for studies on virus entry, identification of entry inhibitors, and immune responses to vaccines. J. Virol. Methods *169*, 365–374.

Wrapp, D., Wang, N., Corbett, K.S., Goldsmith, J.A., Hsieh, C.L., Abiona, O., Graham, B.S., and McLellan, J.S. (2020). Cryo-EM structure of the 2019-nCoV spike in the prefusion conformation. Science *367*, 1260–1263.

Wu, D., Koganti, R., Lambe, U.P., Yadavalli, T., Nandi, S.S., and Shukla, D. (2020). Vaccines and Therapies in Development for SARS-CoV-2 Infections. J. Clin. Med. *9* https://doi.org/10.3390/jcm9061885.

WuDunn, D., and Spear, P.G. (1989). Initial interaction of herpes simplex virus with cells is binding to heparan sulfate. J. Virol. *63*, 52–58.

Xu, D., and Esko, J.D. (2014). Demystifying heparan sulfate-protein interactions. Annu. Rev. Biochem. *83*, 129–157.

Yan, R., Zhang, Y., Li, Y., Xia, L., Guo, Y., and Zhou, Q. (2020). Structural basis for the recognition of SARS-CoV-2 by full-length human ACE2. Science *367*, 1444–1448.

STAR★METHODS

KEY RESOURCES TABLE

REAGENT or RESOURCE	SOURCE	IDENTIFIER
Antibodies		
anti-spike antibody [1A9]	GeneTex	Cat # GTX632604, RRID:AB_2864418
anti-Nucleocapsid antibody	GeneTex	Cat # GTX135357, RRID:AB_2868464
Anti-HS (Clone F58-10E4)	Fisher Scientific	Cat # NC1183789, RRID:AB_2868465
Anti-ACE2	Cell signaling	Cat # 4355S, RRID:AB_2797606
Anti-His-HRP	Genscript	Cat # A00612, RRID:AB_915573
Avidin-HRP	Biolegend	Cat # 405103, RRID:AB_2868466
Streptavadin-Cy5	Thermo Fisher	Cat # SA1011, RRID:AB_2868467
VSV-G antibody	ATCC	Cat # CRL-2700, RRID:AB_2868468
Bacterial and Virus Strains		
SARS-CoV-2 live virus (USA-WA1/2020)	BEI Resources	Cat # NR-52281
VSV-G pseudotyped DG-luciferase or GFP VSV	Kerafast	Cat # EH1020-PM
Chemicals, Peptides, and Recombinant Proteins		
SARS-CoV-2 (2019-nCoV) spike Protein (RBD, His Tag)	Sino Biologicals	Cat # 40592-V08B
SARS-CoV-2 (2019-nCoV) spike S1 + S2 Protein (ECD, His Tag)	Sino Biologicals	Cat # 40589-V08B1
SARS-CoV-2 spike protein (ECD, His & Flag Tag)	GenScript	Cat # Z03481
Critical Commercial Assays		
Bright-Glo™	Promega	Cat # E2610
CellTiter-Blue® assay	Promega	Cat # G8080
Pierce™ Tag Cleavage Enzymes, HRV 3C Protease Solution Kit	Thermo Scientific	Cat # 88946
Deposited Data		
SARS-CoV-2 spike protein RBD	Protein Data Bank	PDB: 6M17
SARS CoV-2 S protein trimer	Protein Data Bank	PDB: 6VSB
SARS CoV-2 S spike protein RBD	Protein Data Bank	PDB: 6M0J
SARS-CoV-1 spike protein RBD	Protein Data Bank	PDB: 3BGF
Experimental Models: Cell Lines		
NCI-H1299	ATCC	Cat # CRL-5803
A549	ATCC	Cat # CCL-185
Hep3B	ATCC	Cat # HB-8064
Hep3B *EXT1*$^{-/-}$	Anower-E-Khuda et al., 2019	N/A
Hep3B *NDST1*$^{-/-}$	Anower-E-Khuda et al., 2019	N/A
Hep3B *HS6ST1/2*$^{-/-}$	Anower-E-Khuda et al., 2019	N/A
A375	ATCC	Cat # CRL-1619
Vero E6	ATCC	Cat # CRL-1586
Human Bronchial Epithelial Cells	Lonza	Cat # CC-2540S
Oligonucleotides		
qPCR primer *ACE2* (human) forward: 5′ – CGAAGCCGAAGACCTGTTCTA - 3′	This paper	N/A
qPCR primer *ACE2* (human) reverse: 5′ – GGGCAAGTGTGGACTGTTCC – 3′	This paper	N/A
qPCR primer *TBP* (human) forward: 5′ – AACTTCGCTTCCGCTGGCCC – 3′	This paper	N/A

(*Continued on next page*)

Continued

REAGENT or RESOURCE	SOURCE	IDENTIFIER
qPCR primer *TBP* (human) reverse: 5′ – GAGGGGAGGCCAAGCCCTGA – 3′	This paper	N/A
guide RNA (sgRNA) targeting *ACE2* (5′- TGGATACATTTGGGCAAGTG –3′)	This paper	N/A
guide RNA targeting *B4GALT7* (5′- TGACCTGCTCCCTCTCAACG-3′)	This paper	N/A
Recombinant DNA		
pαH-SARS-CoV-2 spike	Wrapp et al., 2020	N/A
pVRC-SARS-CoV-2 RBD	Kaneko et al., 2020	N/A
pαH-SARS-CoV-2 spike Mut2 (S383C, D985C)	This paper	N/A
pαH-SARS-CoV-2 spike Mut7 (T883C, V705C)	This paper	N/A
pVRC-SARS-CoV-1 RBD	This paper	N/A
ACE2 expression plasmid	Li et al., 2003	Addgene, plasmid #1786
psPAX2 packaging plasmid	A gift from Didier Trono	Addgene, plasmid #12260
pMD2.g envelope plasmid	A gift from Didier Trono	Addgene, plasmid #12259
lenti-Cas9 plasmid	Sanjana et al., 2014	Addgene, plasmid #52962
Software and Algorithms		
Pymol	Schrödinger	https://pymol.org/2/
ClusPro protein docking server	Kozakov et al., 2013	https://cluspro.bu.edu/publications.php
Molecular operating environment (MOE) software	Chemical Computing Group	https://www.chemcomp.com/Products.htm
The Leginon software	Suloway et al., 2005	https://emg.nysbc.org/redmine/projects/leginon/wiki/Leginon_Homepage
Appion	Lander et al., 2009	https://www.ncbi.nlm.nih.gov/pmc/articles/PMC2775544/
DogPicker	Voss et al., 2009	https://sbgrid.org/software/titles/dogpicker
RELION 3.0	Scheres, 2012	https://github.com/3dem/relion.git
FlowJo	Flowjo	https://www.flowjo.com
Prism 8	Graphpad	https://www.graphpad.com/scientific-software/prism/
ChimeraX	Goddard et al., 2018	https://www.rbvi.ucsf.edu/chimerax/download.html
Other		
EZ-Link™ Sulfo-NHS-Biotin, No-Weigh™	Thermo Fisher Scientific	Cat # A39256
Heparinase I	IBEX	Cat # 60-012
Heparinase II	IBEX	Cat # 60-018
Heparinase II	IBEX	Cat # 60-020
Pierce™ Protein Concentrator PES	Thermo Fisher Scientific	Cat # 88517
Zeba™ Spin Desalting Columns, 40K MWCO, 0.5 mL	Thermo Fisher Scientific	Cat # 87766
APP Heparin	Hikma Pharmaceuticals	N/A
Enoxaparin	Winthrop U.S.	N/A
Heparin hexadecasaccharides	Galen Laboratory Supplies	Cat # HO16
Split glycol heparin	Casu et al., 2004)	N/A
Heparin-BSA	This paper	N/A
MST heparin	TEGA Therapeutics	Cat # rHS09
CHO heparan sulfate	TEGA Therapeutics	Cat # rHS01
1 mL HiTrap heparin-Sepharose column	GE healthcare	Cat # 17-0406-01
PneumaCult-Ex Plus Medium	Stem Cell Tech	Cat # 05040
PneumaCult-ALI Medium	Stem Cell Tech	Cat # 05040

RESOURCE AVAILABILITY

Lead Contact

Further information and request for resources should be directed to the Lead Contact, Thomas Mandel Clausen (tmandelclausen@health.ucsd.edu)

Materials Availability

All developed SARS-CoV-2 expression plasmids produced in this study can be made available upon request to the Lead Contact.

Data and Code Availability

This study did not generate any unique datasets or code.

EXPERIMENTAL MODEL AND SUBJECT DETAILS

Cell Lines

NCI-H1299, A549, Hep3B, A375 and Vero E6 cells were from the American Type Culture Collection (ATCC). NCI-H1299 and A549 cells were grown in RPMI medium, whereas the other lines were grown in DMEM. Hep3B cells carrying mutations in HS biosynthetic enzymes were previously derived from the parent Hep3B line as described (Anower-E-Khuda et al., 2019). All cell media were supplemented with 10% (v/v) FBS, 100 IU/mL of penicillin and 100 μg/mL of streptomycin sulfate, and the cells were grown under an atmosphere of 5% CO_2 and 95% air. Cells were passaged at ~80% confluence and seeded as explained for the individual assays. Protein was produced in ExpiCHO or HEK293-6E cells that were acquired from Thermo Fisher and grown according to the manufacturer's specifications.

Primary Cell Cultures

Human bronchial epithelial cells were acquired from Lonza. They were cultured in PneumaCult-Ex Plus Medium or to PneumaCult-ALI Medium according to the manufacturer's instructions (StemCell Technologies). Specific details on the culture methods are described in the Methods section.

Human Subjects

The collection of human tissue in this study abided by the Helsinki Principles and the General Data Protection Regulation (GDPR) of individual member states. Postmortem human tissues were collected from a deceased individual at the University Hospital at the University of Copenhagen in Denmark. The participant provided consent for the post-mortem tissue to be used for research purposes. All samples were deidentified entirely before transfer to the researchers, and thus did not need IRB approval. The tissue was treated as explained in the Methods section.

METHOD DETAILS

Molecular Modeling

An electrostatic potential map of the SARS-CoV-2 spike protein RBD domain was generated from a crystal structure (PDB:6M17) and visualized using Pymol (version 2.0.6 by Schrödinger). A dp4 fully sulfated heparin fragment was docked to the SARS-CoV-2 spike protein RBD using the ClusPro protein docking server (https://cluspro.org/login.php) (Kozakov et al., 2013, 2017; Vajda et al., 2017). Heparin-protein contacts and energy contributions were evaluated using the Molecular operating environment (MOE) software (Chemical Computing Group).

SARS-CoV-2 spike protein production

Recombinant SARS-CoV-2 spike protein, encoding residues 1-1138 (Wuhan-Hu-1; GenBank: MN908947.3) with proline substitutions at amino acids positions 986 and 987, a "GSAS" substitution at the furin cleavage site (amino acids 682-682), TwinStrepTag and His_{8x} (Wrapp et al., 2020), was produced in ExpiCHO cells by transfection of 6 x10^6 cells/mL at 37°C with 0.8 mg/mL of plasmid DNA using the ExpiCHO expression system transfection kit in ExpiCHO Expression Medium (ThermoFisher). One day later the cells were refed, then incubated at 32°C for 11 days. The conditioned medium was mixed with cOmplete EDTA-free Protease Inhibitor (Roche). Recombinant protein was purified by chromatography on a Ni^{2+} Sepharose 6 Fast Flow column (1 ml, GE LifeSciences). Samples were loaded in ExpiCHO Expression Medium supplemented with 30 mM imidazole, washed in a 20 mM Tris-Cl buffer (pH 7.4) containing 30 mM imidazole and 0.5 M NaCl. Recombinant protein was eluted with buffer containing 0.5 M NaCl and 0.3 M imidazole. The protein was further purified by size exclusion chromatography (HiLoad 16/60 Superdex 200, prep grade. GE LifeSciences) in 20 mM HEPES buffer (pH 7.4) containing 0.2 M NaCl. Recombinant ectodomains migrate as a trimer assuming a monomer molecular mass of ~142,000 and 22 N-linked glycans per monomer (Watanabe et al., 2020). SDS-PAGE, TEM analysis, and SEC studies validate protein purity and the presence of trimers (Figure S2). Recombinant Mut2 (S383C, D985C) and Mut7 (T883C, V705C) were produced in HEK293F cells.

SARS-CoV-2 spike RBD production

SARS-CoV-2 RBD (GenBank: MN975262.1; amino acid residues 319-529) or SARS-CoV-1 RBD (GenBank: AAP13441.1;amino acid residues 355-515) was cloned into pVRC vector containing an HRV 3C protease-cleavable C-terminal TwinStrepTag and His_{8x} and the sequence was confirmed (Kaneko et al., 2020). Recombinant protein was expressed by transient transfection of mammalian Expi293F suspension cells. Supernatants were harvested 5 days post-transfection and passed over Cobalt-TALON resin (Takara) followed by size exclusion chromatography on Superdex 200 Increase 10/300 GL (GE Healthcare) in PBS. Purity was assessed by SDS-PAGE analysis. Some initial optimization experiments utilized recombinant SARS-CoV-2 RBD and recombinant SARS-CoV-2 spike extracellular domain purchased from Sino Biological and Genscript. SDS-PAGE and SEC analysis is included in Figure S2.

Transmission electron microscopy

Samples of the recombinant trimeric spike protein ectodomain were diluted to 0.03 mg/mL in 1X TBS pH 7.4. Carbon coated copper mesh grids were glow discharged and 3 mL of the diluted sample was placed on a grid for 30 s then blotted off. Uniform stain was achieved by depositing 3 mL of uranyl formate (2%) on the grid for 55 s and then blotted off. Grids were transferred to a Thermo Fisher Morgagni operating at 80 kV. Images at 56,000 magnification were acquired using a MegaView 2K camera via the RADIUS software. A dataset of 138 micrographs at 52,000x magnification and −1.5 mm defocus was collected on a FEI Tecnai Spirit (120keV) with a FEI Eagle 4k by 4k CCD camera. The pixel size was 2.06 Å per pixel and the dose was 25 $e^-/Å^2$. The Leginon (Suloway et al., 2005) software was used to automate the data collection and the raw micrographs were stored in the Appion (Lander et al., 2009) database. Particles on the micrographs were picked using DogPicker (Voss et al., 2009), stack with a box size of 200 pixels, and 2D classified with RELION 3.0 (Scheres, 2012).

Recombinant ACE2 expression and purification

Secreted human ACE2 was transiently produced in suspension HEK293-6E cells. A plasmid encoding residues 1-615 of ACE2 with a C-terminal HRV-3C protease cleavage site, a TwinStrepTag and an His_{8x} Tag was a gift from Jason S. McLellan, University of Texas at Austin. Briefly, 100 mL of HEK293-6E cells were seeded at a cell density of 0.5 × 10^6 cells/mL 24 h before transfection with polyethyleneimine (PEI). For transfection, 100 μg of the ACE2 plasmid and 300 μg of PEI (1:3 ratio) were incubated for 15 min at room temperature. Transfected cells were cultured for 48 h and fed with 100 mL fresh media for additional 48 h before harvest. Secreted ACE2 were purified from culture medium by Ni-NTA affinity chromatography (QIAGEN). Filtered media was mixed 3:1 (v/v) in 4X binding buffer (100 mM Tris-HCl, pH 8,0, 1,2 M NaCl) and loaded on to a self-packed column, pre-equilibrated with washing buffer (25 mM Tris-HCl, pH 8, 0.3 M NaCl, 20 mM imidazole). Bound protein was washed with buffer and eluted with 0.2 M imidazole in washing buffer. The protein containing fractions were identified by SDS-PAGE.

Analytical Heparin-Sepharose Chromatography

SARS-CoV-2 spike protein in dPBS was applied to a 1 mL HiTrap heparin-Sepharose column (GE Healthcare). The column was washed with 5 mL of dPBS and bound protein was eluted with a gradient of NaCl from 150 mM to 1 M in dPBS.

Biotinylation

For binding studies, recombinant spike protein and ACE2 was conjugated with EZ-Link™ Sulfo-NHS-Biotin (1:3 molar ratio; Thermo Fisher) in Dulbecco's PBS at room temperature for 30 min. Glycine (0.1 M) was added to quench the reaction and the buffer was exchanged for PBS using a Zeba spin column (Thermo Fisher).

Binding of spike protein to heparin

Heparin (APP Pharmaceuticals) (50 ng) in 5 μL solution each was pipetted into each well of a high binding plate. A set of wells were set up without heparin. A solution (0.2 mL) of 90% saturated (3.7 M) ammonium sulfate was added to each well and incubated overnight to immobilize the HS. The next day, the wells were washed twice with 0.2 mL of PBS then blocked with 0.2 mL of PBS containing 0.1% Tween 20 (PBST) and 0.1% BSA for 1 h at room temperature. The wells were emptied and 45 μL of PBST/BSA with 0, 1, 3, 6, 10, 30, 60 or 100 nM of his/FLAG-tagged SARS-CoV-2 spike protein (GenScript, Z03481-100) was added to each well. The wells were incubated for 1 h at room temperature, washed thrice with 0.2 mL of PBST, and then incubated with 45 mL each of 0.1 μg/mL of THE anti-his-HRP (GenScript, A00612) in PBST/BSA for 1 h at room temperature. The wells were washed 5 times with 0.2 mL of PBST. TMB Turbo substrate was added to each well (0.1 mL), and the color was allowed to develop. The reaction was quenched by addition of 0.1 mL of 1 M sulfuric acid. The absorbance was measured by 450 nm.

Immobilization and binding of ACE2, spike and heparin-BSA

High binding microtiter plates were coated with heparin-BSA (100 ng/well), ACE2 (150 ng/well), or S protein (200 ng/well) overnight at 4°C. The plates were then blocked for 3 h at 37°C with TSM buffer (20 mM Tris buffer, pH 7.4, containing 150 mM NaCl, 2 mM $MgCl_2$, 2 mM $CaCl_2$, 0.05% Tween-20, and 1% BSA) and a dilution series of biotinylated proteins prepared in TSM buffer was added to the plates in triplicate. Bound biotinylated protein was detected by adding Avidin-HRP (405103, BioLegend) diluted 1:2000 in TSM buffer. Lastly, the plates were developed with TMB turbo substrate for 5-15 min. The reaction was quenched using 1 M sulfuric acid and the

absorbance was measured at 450 nm. To detect the formation of a ternary complex of ACE2, S protein and heparin-BSA, the plates were first coated with heparin BSA and incubated with S protein (100 nM). ACE2 binding was measured to bound spike protein as described above.

Negative stain-electron microscopy to visualize the spike, ACE2, and heparin interaction

Mixtures of stabilized (Mut7) spike protein, 6x molar excess soluble ACE2 ectodomain, with or without 9x molar excess an icosasaccharide (dp20) fragment derived from heparin were incubated at 4°C for 15 min or 1 h. Samples were diluted to 0.02 mg/mL with respect to spike protein in 1X PBS pH 7.4. Carbon coated copper mesh grids were glow discharged at 20 mA for 30 s and 3 mL sample was applied for 20 s and blotted off. Grids were washed five times in 10 mL 1X TBS pH 7.4 for 15 s then stained and blotted twice with 3 mL 2% uranyl formate for 15 s. Grids were imaged with an FEI Tecnai Spirit (120 keV) or FEI Tecnai F20 (200 keV) with an FEI Eagle CCD (4k) camera. Data were collected on the FEI Tecnai F20 at 62,000x magnification, −1.5 mm defocus with a pixel size of 1.77 Å per pixel. These datasets employed a box size of 256 and comprised 167 to 331 micrographs. Data were collected on the FEI Tecnai Spirit as described above. Data collection on both microscopes was automated through Leginon (Suloway et al., 2005). Stored in the Appion (Lander et al., 2009) database, and particles were picked with DoG Picker (Voss et al., 2009). Particles were 2D classified with RELION 3.0 (Scheres, 2012). Trimeric 2D classes were selected for iterative 3D classification with RELION 3.0. Classifications were performed until 3D classes demonstrated ACE2 occupancy throughout the relevant threshold-level of the spike protein as visualized using ChimeraX (Goddard et al., 2018). Particle counts of final 3D classes were obtained with RELION 3.0 (Scheres, 2012) and the percentages of particles bound to 0, 1, 2, or 3 ACE2 were calculated and visualized in GraphPad Prism 8.

Flow cytometry

Cells at 50%–80% confluence were lifted with PBS containing 10 mM EDTA (GIBCO) and washed in PBS containing 0.5% BSA. The cells were seeded into a 96-well plate at 10^5 cells per well. In some experiments, a portion of the cells was treated with HSase mix (2.5 mU/mL HSase I, 2.5 mU/mL HSase II, and 5 mU/mL HSase III; IBEX) for 30 min at 37°C in PBS containing 0.5% BSA. They were incubated for 30 min at 4°C with biotinylated spike protein (S1/S2 or RBD; 20 μg/mL or serial dilutions) in PBS containing 0.5% BSA. The cells were washed twice and then reacted for 30 min at 4°C with Streptavadin-Cy5 (Thermo Fisher; 1:1000 dilution) in PBS containing 0.5% BSA,. The cells were washed twice and then analyzed using a FACSCalibur or a FACSCanto instrument (BD Bioscience). All experiments were done a minimum of three separate times in three technical replicates. Data analysis was performed using FlowJo software and statistical analyses were done in Prism 8 (GraphPad).

HS purification from tissues

Fresh human tissue was washed in PBS, frozen, and lyophilized. The dried tissue was crushed into a fine powder, weighed, resuspended in PBS containing 1 mg/mL Pronase (Streptomyces griseus, Sigma Aldrich) and 0.1% Triton X-100, and incubated at 37°C overnight with shaking. The samples were centrifuged at 20,000 x g for 20 min and the supernatant was mixed 1:10 with equilibration buffer (50 mM sodium acetate, 0.2 M NaCl, 0.1% Triton X-100, pH 6) and loaded onto a DEAE Sephacel column (GE healthcare) equilibrated with buffer. The column was washed with 50 mM sodium acetate buffer containing 0.2 M NaCl, pH 6.0, and bound GAGs were eluted with 50 mM sodium acetate buffer containing 2.0 M NaCl, pH 6.0. The eluate was mixed with ethanol saturated with sodium acetate (1:3, vol/vol) and kept at −20°C overnight, followed by centrifugation at 20,000 x g at 4°C for 20 min. The pellets were dried in a centrifugal evaporator and reconstituted in DNase buffer (50 mM Tris, 50 mM NaCl, 2.5 mM $MgCl_2$, 0.5 mM $CaCl_2$, pH 8.0) with 20 kU/mL bovine pancreatic deoxyribonuclease I (Sigma Aldrich) and incubated with shaking for 2 h at 37°C. The samples were adjusted to 50 mM Tris and 50 mM NaCl, pH 8.0, and incubated for 4 h at 37°C with 20 mU/mL chondroitinase ABC (Proteus vulgaris, Sigma Aldrich). The HS was purified over a DEAE column and precipitated with 90% ethanol (Esko, 1993).

HS digestion and LC-MS analysis

For HS quantification and disaccharide analysis, purified HS was digested with a mixture of heparin lyases I-III (2 mU each) for 2 h at 37°C in 40 mM ammonium acetate buffer containing 3.3 mM calcium acetate, pH 7.0. The samples were dried in a centrifugal evaporator and reductively aminated at 37°C for 16 h with 17 μl [$^{12}C_6$]aniline or [$^{13}C_6$]aniline and 17 mL of 1 M $NaCNBH_3$ (Sigma-Aldrich) freshly prepared in dimethyl sulfoxide:acetic acid (7:3, v/v) (Lawrence et al., 2008). The samples were dried in a centrifugal evaporator and reconstituted in 16 μl Pierce LC-MS grade water (Thermo Scientific). For LC-MS analysis, 5 μl of the [$^{12}C_6$]aniline-tagged samples were mixed with 1 μl LC-MS buffer (80 mM acetic acid and 50 mM of the ion pairing agent dibutylamine (DBA, Sigma-Aldrich)), 1 μl of internal [$^{13}C_6$]aniline-tagged HS dp2 standards, and 3 μl LC-MS grade water.

The derivatized HS disaccharides were analyzed by LC-MS with an LTQ Orbitrap Discovery electrospray ionization mass spectrometer (Thermo Scientific) equipped with an Ultimate 3000 quaternary HPLC pump (Dionex). The samples were separated on a reverse phase column (TARGA C18, 150 mm x 1.0 mm diameter, 5 μm beads; Higgins Analytical, Inc.) and ions were monitored in negative mode. The isocratic steps were: 100% buffer A (8 mm acetic acid, 5 mm DBA) for 10 min; 17% buffer B (70% methanol, 8 mm acetic acid, 5 mm DBA) for 10 min; 32% buffer B for 15 min; 40% buffer B for 15 min; 50% buffer B for 15 min; 60% buffer B for 15 min; 100% buffer B for 10 min; and 100% buffer A for 10 min. The capillary temperature and spray voltage were kept at 140°C and 4.75 kV, respectively. The accumulative extracted ion current (XIC) was computed, and further data analysis was carried out as described in the documentation for the Qual Browser software provided by Thermo-Finnigan.

ACE2 overexpression and immunoblotting

The ACE2 expression plasmid (Addgene, plasmid #1786) (Li et al., 2003) was received in bacteria and purified with a maxiprep kit (Zymogen). A375 wild-type and *B4GALT7*$^{-/-}$ cells were transfected with 15 μg ACE2 expression plasmid in a mixture of DMEM, OptiMEM (GIBCO), Lipofectamine 2000 with Plus reagent (Invitrogen). After 4 h, the medium was replaced with DMEM/10% FBS and the cells were incubated for 3 d before being used for experiments.

To measure ACE2 expression, cells were lysed in RIPA Buffer (Millipore, 20-188) with protease inhibitors (cOmplete, Mini, EDTA-free Protease Inhibitor Cocktail, Roche, 11836170001). The lysates were incubated on ice for 1 h and then centrifuged for 10 min at 10,000 x g at 4 þC. The supernated was collected and protein was quantified by BCA assay (Pierce BCA Protein Assay Kit Thermo-Fisher Scientific, 23225). To measure ACE2 expression in transfected cells, 4ug of each cell lysate was run on SDS-PAGE in triplicate. A protein ladder (PageRule Plus Pre-stained Protein Ladder, Thermo Scientific, PI26619) was used for size determination. To measure endogenous levels of hACE2 in cell lines, 15 μg of each cell lysate was used. Samples were separated by electrophoresis on a 15-well Bolt 4%–12% Bis-Tris gel (Invitrogen, NW04125 or Invitrogen, NP0336) in NuPAGE MOPS SDS Running Buffer (Invitrogen, NP0001). The gels were transferred onto a PVDF membrane (Immobilon-FL PVDF Membrane, Millipore, IPFL0010) in NuPAGE Transfer Buffer (Invitrogen, NP00061). The membranes were blocked 1 h at room temperature with Odyssey PBS Blocking Buffer (Li-Cor, 927-40000) or in 5% Blotting-Grade Blocker (Biorad, 1706404) in TBST (50 mM Tris buffer, pH 7.5 containing 150 mM NaCl and 0.1% Tween-20) and then incubated overnight at 4 þC with anti-hACE2 antibody (1:1000 or 1:500; R&D AF933) and anti-beta actin (1:2000; CST 4970) in 5% BSA (Sigma-Aldrich A9647) or 2.5% Blotting-Grade Blocker in TBST. The blot was incubated at room temperature for 1 h with appropriate secondary antibodies (Donkey anti-Goat, Li-Cor, 926-32214; IRDye 680LT Donkey anti-Rabbit, Li-Cor, 926-68023; both at 1:20,000) in 5% BSA or 2.5% Blotting-Grade Blocker and 0.02% SDS in TBST. The blots were imaged using an Odyssey Infrared Imaging System (Li-Cor) and quantified using the companion ImageStudio software.

qPCR

mRNA was extracted from the cells using TRIzol (Invitrogen) and chloroform and purified using the RNeasy Kit (QIAGEN). cDNA was synthesized from the mRNA using random primers and the SuperScript III First-Strand Synthesis System (Invitrogen). SYBR Green Master Mix (Applied Biosystems) was used for qPCR following the manufacturer's instructions, and the expression of TBP was used to normalize the expression of *ACE2* between the samples. The qPCR primers used were as follows: *ACE2* (human) forward: 5′ – CGAAGCCGAAGACCTGTTCTA - 3′ and reverse: 5′ – GGGCAAGTGTGGACTGTTCC – 3′; and *TBP* (human) forward: 5′ – AACTTCGCTTCCGCTGGCCC – 3′ and reverse: 5′ – GAGGGGAGGCCAAGCCCTGA – 3′.

Mutant cell line generation

To generate the Cas9 lentiviral expression plasmid, 2.5 × 10^6 HEK293T cells were seeded to a 10-cm diameter plate in DMEM supplemented with 10% FBS. The following day, the cells were co-transfected with the psPAX2 packaging plasmid (Addgene, plasmid #12260), pMD2.g envelope plasmid (Addgene, plasmid #12259), and lenti-Cas9 plasmid (Addgene, plasmid #52962) (Sanjana et al., 2014) in DMEM supplemented with Fugene6 (30μL in 600μL DMEM). Media containing the lentivirus was collected and used to infect A549 WT and A375 WT cells, which were subsequently cultured with 5 μg/mL and 2 μg/mL blasticidin, respectively, to select for stably transduced cells. A single guide RNA (sgRNA) targeting *ACE2* (5′- TGGATACATTTGGGCAAGTG −3′) and one targeting *B4GALT7* (5′- TGACCTGCTCCCTCTCAACG-3′) was cloned into the lentiGuide-Puro plasmid (Addgene plasmid #52963) following published procedure (Sanjana et al., 2014). The lentiviral sgRNA construct was generated in HEK293T cells, using the same protocol as for the Cas9 expression plasmid, and used to infect A549-Cas9 and A375-Cas9 cells to generate CRISPR knockout mutant cell lines. After infection, the cells were cultured with 2 μg/mL puromycin to select for cells with stably integrated lentivirus. After 7 d, the cells were serially diluted into 96-well plates. Single colonies where expanded and DNA was extracted using the DNeasy blood and tissue DNA isolation kit (QIAGEN). Proper editing was verified by sequencing (Genewiz Inc.) and gene analysis using the online ICE tool from Synthego (Figure S5).

Preparation and infection by pseudotyped VSV

Vesicular Stomatitis Virus (VSV) pseudotyped with spike proteins of SARS-CoV-2 were generated according to a published protocol (Whitt, 2010). Briefly, HEK293T, transfected to express full length SARS-CoV-2 spike proteins, were inoculated with VSV-G pseudotyped DG-luciferase or GFP VSV (Kerafast, MA). After 2 h at 37°C, the inoculum was removed and cells were refed with DMEM supplemented with 10% FBS, 50 U/mL penicillin, 50 μg/mL streptomycin, and VSV-G antibody (I1, mouse hybridoma supernatant from CRL-2700; ATCC). Pseudotyped particles were collected 20 h post-inoculation, centrifuged at 1,320 × g to remove cell debris and stored at −80°C until use.

Cells were seeded at 10,000 cells per well in a 96-well plate. The cells (60%–70% confluence) were treated with HSases for 30 min at 37°C in serum-free DMEM. Culture supernatant containing pseudovirus (20-100 μL) was adjusted to a total volume of 100 μL with PBS, HSase mix or the indicated inhibitors and the solution was added to the cells. After 4 h at 37°C the media was changed to complete DMEM. The cells were then incubated for 16 h to allow expression of reporter gene. Cells infected with GFP containing virus were visualized by fluorescence microscopy and counted by flow cytometry. Cells infected with Luciferase containing virus were analyzed by Bright-Glo™ (Promega) using the manufacturers protocol. Briefly, 100 μL of luciferin lysis solution was added to the cells

and incubated for 5 min at room temperature. The solution was transferred to a black 96-well plate and luminescence was detected using an EnSpire multimodal plate reader (Perkin Elmer). Data analysis and statistical analysis was performed in Prism 8.

Infection by authentic SARS-CoV-2 virus

SARS-CoV-2 isolate USA-WA1/2020 (BEI Resources, #NR-52281) was propagated and infectious units quantified by plaque assay using Vero E6 cells. The cells were treated with or without HSase mix (IBEX Pharmaceuticals) or with unfractionated heparin (UFH) and infected with SARS-CoV-2 for 1 h at 37°C. HSase-treated Vero E6 cells were incubated with HSase mix 30 min prior to infection until 24 h post-infection or with UFH at the indicated concentrations from the start of infection until 24 h post-infection. The cells were washed twice with PBS, lifted in Trypsin-EDTA (GIBCO), and fixed in 4% formaldehyde for 30 min. Cells were permeabilized for flow cytometry using BD Cytofix/Cytoperm according to the manufacturers protocol for fixed cells and stained with anti-spike antibody [1A9] (GeneTex GTX632604) and anti-Nucleocapsid antibody (GeneTex GTX135357) that were directly conjugated with Alexa Fluor 647 and Alexa Fluor 594 labeling kits (Invitrogen), respectively. Zombie UV was used to gate for live cells in the analysis. Cells were then analyzed using an MA900 Cell Sorter (Sony).

Virus plaque assays

Confluent monolayers of Vero E6 or Hep3B cells were infected with SARS-CoV-2 at an MOI of 0.1. After one h of incubation at 37°C, the virus was removed, and the medium was replaced. After 48 h, cell culture supernatants were collected and stored at −80°C. Virus titers were determined by plaque assays on Vero E6 monolayers. In short, serial dilutions of virus stocks in Minimum Essential Media MEM medium (GIBCO, #41500-018) supplemented with 2% FBS was added to Vero E6 monolayers on 24-well plates (Greiner bio-one, #662160) and rocked for 1 h at room temperature. The cells were subsequently overlaid with MEM containing 1% cellulose (Millipore Sigma, #435244), 2% FBS, and 10 mM HEPES buffer, pH 7.5 (Sigma #H0887) and the plates were incubated at 37°C under an atmosphere of 5% CO_2/95% air for 48 h. The plaques were visualized by fixation of the cells with a mixture of 10% formaldehyde and 2% methanol (v/v in water) for 2 h. The monolayer was washed once with PBS and stained with 0.1% Crystal Violet (Millipore Sigma # V5265) prepared in 20% ethanol. After 15 min, the wells were washed with PBS, and plaques were counted to determine the virus titers. All work with the SARS-CoV-2 was conducted in Biosafety Level-3 conditions either at the University of California San Diego or at the Eva J Pell Laboratory, The Pennsylvania State University, following the guidelines approved by the Institutional Biosafety Committees.

Human bronchial epithelial cell air-liquid interface generation and infection

Human Bronchial Epithelial Cells (HBECs, Lonza) were cultured in T75 flasks in PneumaCult-Ex Plus Medium according to manufacturer instructions (StemCell Technologies). To generate air-liquid interface (ALI) cultures, HBECs were plated on collagen I-coated 24 well transwell inserts with a 0.4-micron pore size (Costar, Corning) at $5x10^4$ cells/mL. Cells were maintained for 3-4 days in PneumaCult-Ex Plus Medium until confluence, then changed to PneumaCult-ALI Medium (StemCell Technologies) containing ROCK inhibitor (Y-27632, Tocris) for 4 days. Fresh medium, 100 μl in the apical chamber and 500 μl in the basal chamber, was added daily. At day 7, the medium in the apical chambers was removed, and the basal chambers were changed every 2-3 days with apical washes with PBS every week for 28 days.

The apical side of the HBEC ALI culture was gently washed three times with 200 μl of phosphate buffered saline without divalent cations (PBS−/−). Heparinase was added to the apical side for half an h prior to infection. An MOI of 0.5 of authentic SARS-CoV-2 live virus (USA-WA1/2020 (BEI Resources, #NR-52281)) in 100 μl total volume of PBS was added to the apical chamber with either DMSO, Heparinase (2.5mU/mL heparin lyase II, and 5mU/mL heparin lyase III (IBEX)) or 100ug/mL of Unfractionated Heparin. Cells were incubated at 37C and 5% CO2 for 4 h. Unbound virus was removed, the apical surface was washed and the compounds were re-added to the apical chamber. Cells were incubated for another 20 h at 37C and 5% CO2. After inoculation, cells were washed once with PBS−/− and 100 μl TrypLE (ThermoFisher) was added to the apical chamber then incubated for 10 min in the incubator. Cells were gently pipetted up and down and transferred into a sterile 15 mL conical tube containing neutralizing medium of DMEM + 3% FBS. TrypLE was added again for 3 rounds of 10 min for a total of 30 min to clear transwell membrane. Cells were spun down and resuspended in PBS with Zombie UV viability dye for 15 min in room temp. Cells were washed once with FACS buffer then fixed in 4% PFA for 30 min at room temp. PFA was washed off and cells were resuspended in PBS. Zombie UV was used to gate for live cells in the analysis. Infection was analyzed by flow cytometry as explained above.

Cell Viability Assay

Cell viability was assessed using the CellTiter-Blue® assay (Promega). Briefly, Vero cells were seeded into a 96 well plate. The cells were treated with HSase mix (2.5 mU/mL HSase II, and 5 mU/mL HSase III; IBEX) or 100 μg/mL UFH for 16 h. The viability of the cells using CellTiter-Blue® was measured according to the manufacturers protocol. Briefly, the CellTiter-Blue® reagent was added directly to the cell culture and the cells were incubated overnight. Fluorescence was read at excitation 560nm and emission 590nm, using an EnSpire multimodal plate reader (Perkin Elmer). Data analysis was performed in Prism. The human Bronchial epithelial cells were grown at an air-liquid interface as explained above. Cell viability after treatment with HSase mix (2.5 mU/mL HSase II, and 5 mU/mL HSase III; IBEX) or 100 μg/mL UFH for 16 h was measured by adding CellTiter-Blue® reagent directly to the transwell inserts and developed as explained above.

QUANTIFICATION AND STATISTICAL ANALYSIS

All statistical analyses were performed in Prism 8 (Graphpad). All experiments were performed in triplicate and repeated as indicated in the figure legends. Data was analyzed statistically using unpaired t tests when two groups were being compared or by one-way ANOVA without post hoc correction for multiple comparisons. IC_{50} values and confidence intervals were determined using non-linear regression using the inhibitor versus response least-squares fit algorithm. The error bars in the figures refer to mean plus standard deviation (SD) values. The specific statistical tests used are listed in the figure legends and in the methods section. Experiments were evaluated by statistical significance according to the following scheme; ns: $p > 0.05$, *: $p \leq 0.05$, **: $p \leq 0.01$, ***: $p \leq 0.001$, ****: $p \leq 0.0001$.

Supplemental Figures

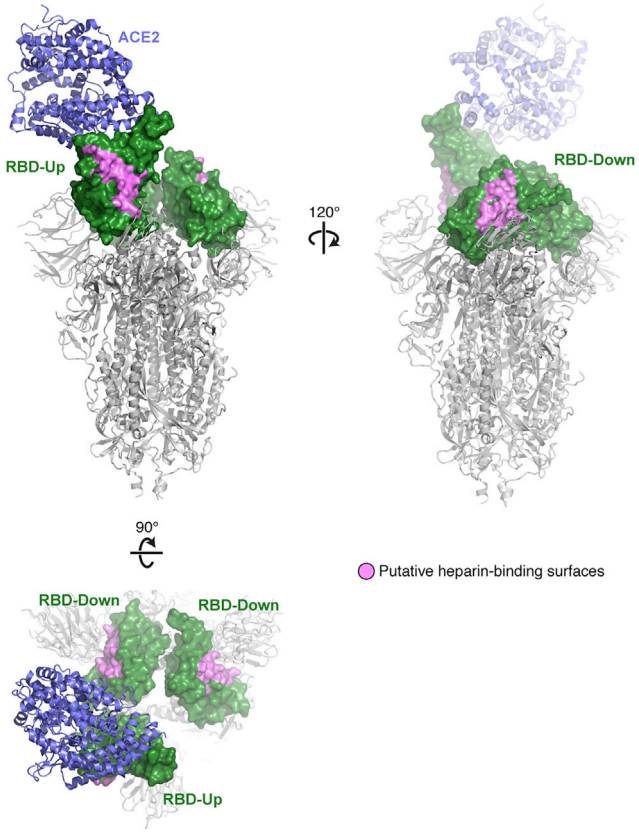

Figure S1. Location of the Putative Heparin/HS Binding Site in the Spike Protein RBD from SARS-CoV-2, Related to Figure 1

PDB files 6VSB and 6M0J were used to model the spike protein. The residues colored pink on the three RBDs (444+509+346+354+356+357+355+466+347+348+349+353+450+448+451+352) make up a potential binding site for heparin and heparan sulfate.

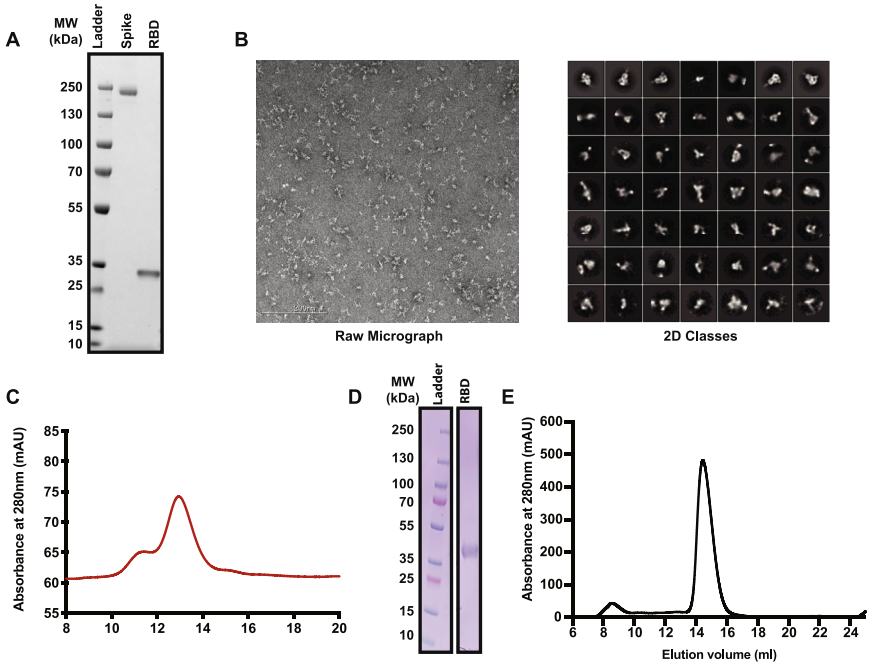

Figure S2. Analysis of Recombinant Spike Proteins and Receptor-Binding Domain, Related to Star Methods, Protein Production

(A) SDS-PAGE gel of recombinant SARS-CoV-2 spike ectodomain protein produced in ExpiCho cells and commercial recombinant SARS-CoV-2 RBD.

(B) Transmission electron micrographs of recombinant SARS-CoV-2 spike ectodomain protein.

(C) Size exclusion chromatography of recombinant SARS-CoV-2 spike ectodomain protein on a Superose 6 column.

(D) SDS-PAGE gel of recombinant SARS-CoV-2 RBD produced in ExpiHEK cells.

(E) Size exclusion chromatography of recombinant SARS-CoV-2 RBD on a Superdex200 column.

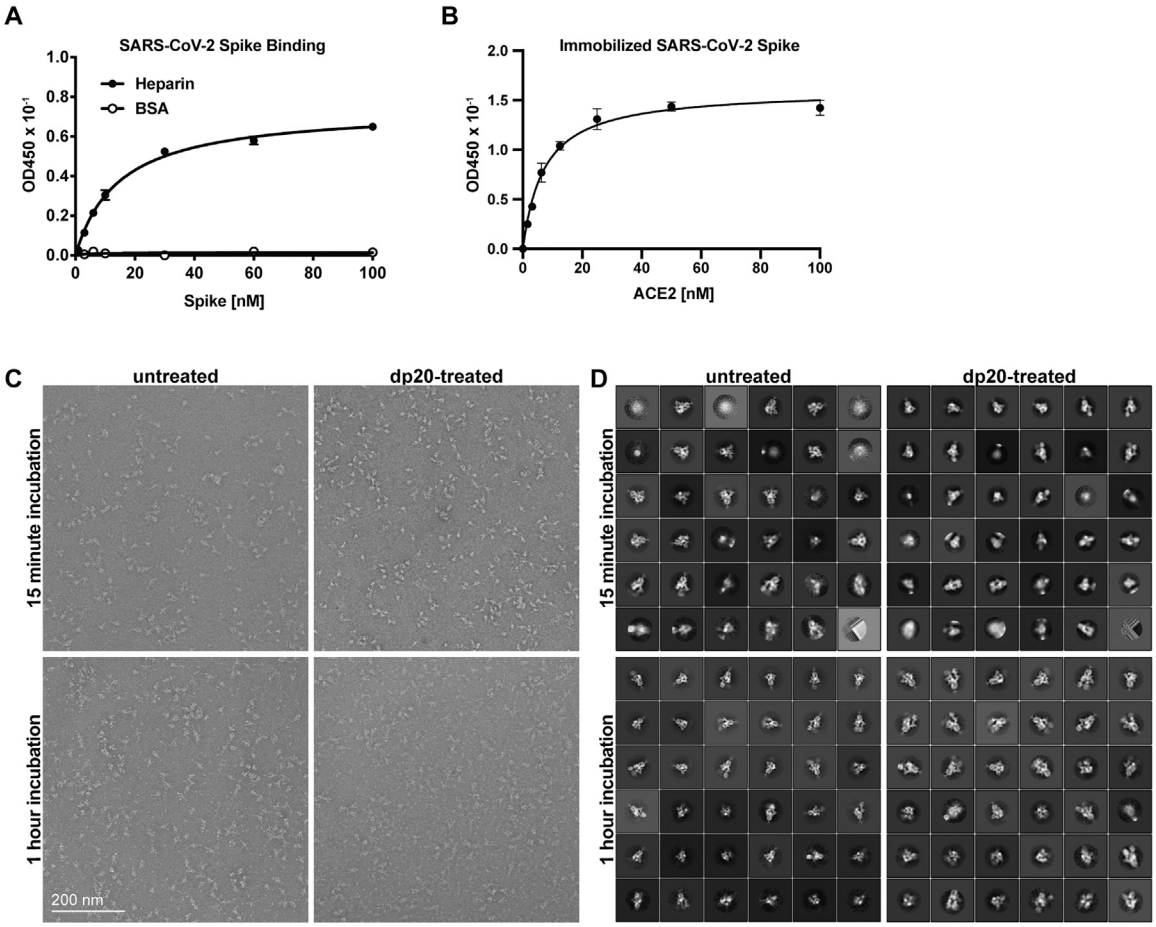

Figure S3. Binding of Spike Protein to Heparin and ACE2 and Electron Micrographs of the Spike-ACE2 Complexes, Related to Figure 2

(A) SARS-CoV-2 spike binding to immobilized heparin or BSA.

(B) ACE2 binding to immobilized spike protein.

(C) Transmission electron micrographs of stabilized spike protein treated with ACE2 and with or without dp20 for 15 min or 1 h.

(D) 2D classes averages for each condition.

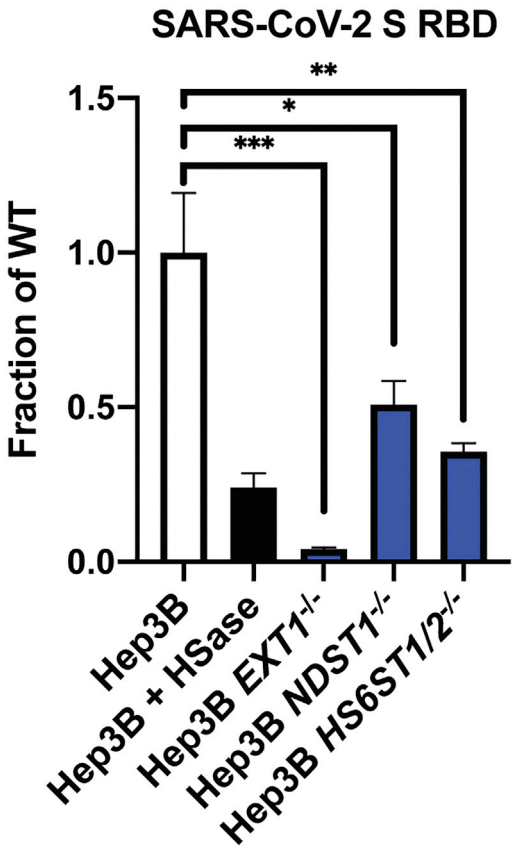

Figure S4. Binding of RBD Protein to Hep3B Mutants, Related to Figure 3

Binding of SARS-CoV-2 S RBD protein (20 μg/mL) to Hep3B mutants. Binding was measured by flow cytometry. Statistical analysis by unpaired t test. (ns: $p > 0.05$, *: $p \leq 0.05$, **: $p \leq 0.01$, ***: $p \leq 0.001$, ****: $p \leq 0.0001$).

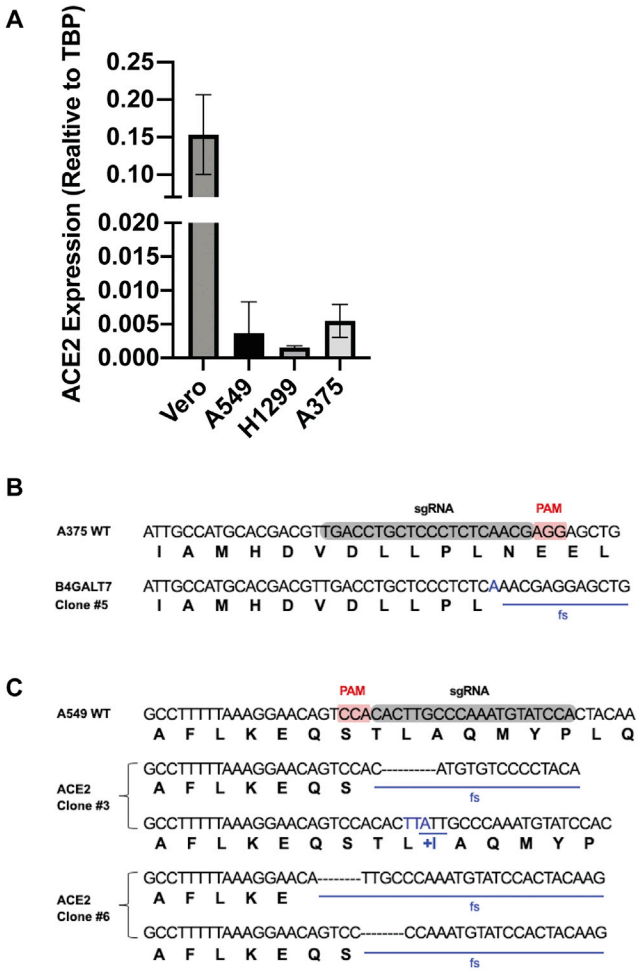

Figure S5. ACE2 Expression and Mutations, Related to Figure 5

(A) qRT-PCR analysis of ACE2 expression.

(B) DNA sequencing of ACE2 mutant alleles in A375 mutants.

(C) DNA sequencing of ACE2 mutant alleles in A549 mutants.

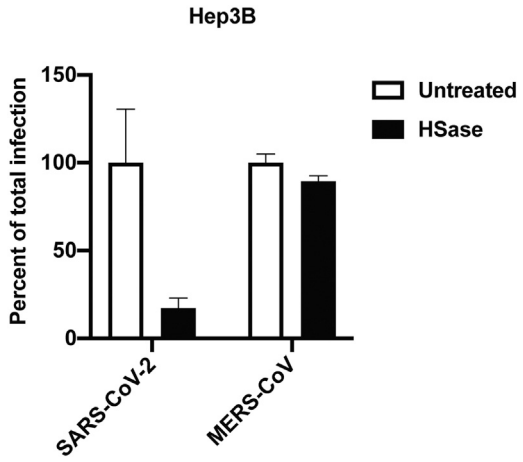

Figure S6. Infection of Hep3B by MERS Pseudovirus, Related to Figure 6

Infection of Hep3B cells with SARS-CoV-2 and MERS-CoV S protein pseudotyped viruses carrying luciferase with and without treatment with heparin lyases.

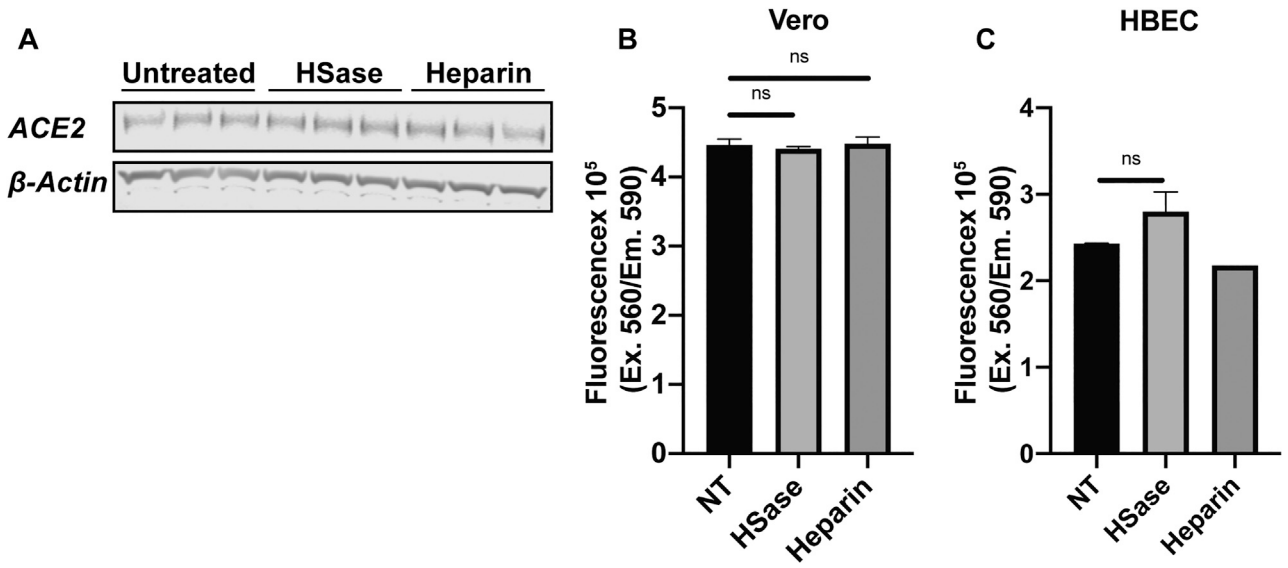

Figure S7. Heparin and Heparin Lyases Have No Effect on ACE2 Expression or Cell Viability, Related to Figure 7

(A) Western blot analysis of ACE2 expression in Vero E6 cells treated with heparin lyases or 100 μg/mL UFH.

(B and C) Assessment of cell viability after treatment with heparin lyase or 100 μg/mL UFH for 16 h in Vero (B) and human bronchial epithelial cells (HBEC) (C). Cell viability was measured using CellTiter-Blue. Statistical analysis by unpaired t test. (ns: $p > 0.05$, *: $p \leq 0.05$, **: $p \leq 0.01$, ***: $p \leq 0.001$, ****: $p \leq 0.0001$).